PHYSICAL REVIEW A VOLUME 14, NUMBER 6 DECEMBER 1976

# Microwave EPR self-induced transparency*

S. B. Grossman† and E. L. Hahn
*Department of Physics, University of California, Berkeley, California 94720*
(Received 16 August 1976)

The waveguide propagation of a microwave magnetic field pulse at electron paramagnetic resonance (EPR) with a free radical sample of electron spins distributed along the guide displays the phenomenon of self-induced transparency (SIT). Predictions of plane-wave optical SIT are modified by summation of the magnetic-moment–microwave-field coupling over the transverse waveguide mode for specific sample geometries. Mode modified pulse area theorems are presented. Observed output pulse areas and shapes are compared with computer predictions. After pulse propagation over several absorption lengths a spontaneous zero-area pulse propagation effect is observed for a short weak input pulse with spectral width comparable to or larger than the spin-resonance linewidth. Alternating 180° phase shifts in the pulse carrier wave, accounting for zero area, signify magnetic dipole transitions which alternate between coherent absorption and emission to some extent, and therefore anomalous pulse propagation is observed. For pulses applied off-resonance, linear and nonlinear shifts of the average carrier frequency occur toward the center of the spin resonance.

## I. INTRODUCTION

Except for the pulse-propagation effect of self-induced transparency[1] (SIT), a number of pulsed-laser coherent phenomena are close analogs of earlier transient cavity spin-resonance experiments. Optical electric dipole transient nutations, photon echos, adiabatic inversion, and beat oscillations of various kinds reflect primarily the time dependence of coherent superposition states. Propagation becomes a secondary consideration for samples of low density and dimensions less than the classical absorption length. These effects are well described by the Bloch type of nuclear-magnetic-resonance (NMR) equations[2] adapted to the two-quantum level problem.[3]

In this investigation we present the results of a direct electron paramagnetic spin resonance (EPR) self-induced transparency experiment.[4] Here the effect of anomalous microwave pulse propagation occurs for a direct magnetic-moment–microwave-field interaction over distances of pulse propagation exceeding many wavelengths and several classical absorption lengths. A traveling microwave pulse is matched into a waveguide which contains a free-radical sample of electron spins polarized in a constant magnetic field $H_0$. The pulse carrier frequency is near or at electron paramagnetic resonance in the $x$-band region (9.3–11.7 GHz). The output pulse shape, intensity, and spectral properties are monitored as a function of input pulse conditions. Microwave EPR techniques permit flexibility of tuning on- and off-resonance, high pulse repetition rate, and accurate pulse-spectrum analysis far superior to equivalent measurements of short pulses at optical frequencies. This flexibility enables more detailed and controlled experimental studies of non-plane-wave conditions, phase modulation effects, and zero-area pulse propagation.[5] All of these effects relate to fundamental aspects of SIT also observed.

The ultrasonic SIT experiment of Shiren[6] is the only previous microwave type of SIT experiment which presents advantages similar to the direct EPR experiment reported here. The main difference is that traveling-wave ultrasonic pulses are first generated by microwave pulses. The ultrasonic pulses in turn are coupled into a crystal and interact with a two-level spin system. Since the EPR experiment involves direct microwave coupling to the spin system, the problems of microwave power matching and pulse reflections are easier to overcome than in the ultrasonic case. Also the mode of microwave pulse propagation is better known and controlled in the EPR case. A primary disadvantage of the EPR experiment results from the relatively weak direct coupling of spin magnetic moments with a microwave field compared to strong coupling in laser or ultrasonic pulse experiments. Therefore, large waveguide sample lengths in spiral form (~100 cm) must be fitted between the magnet pole pieces to provide a sufficient number of absorption lengths necessary for SIT.

The coupling of spin magnetic moments with a microwave magnetic field in a waveguide involves the unique constraint of waveguide mode. For ideal SIT in its simplest form,[1] a pulse propagates as a plane wave in which transient induced absorption and emission during the first and second halves of the pulse, respectively, balance one another. With no losses present, a distortionless pulse evolves with an area (product of field amplitude and pulse width) given by $2\pi$ and with a hyperbolic secant shape. In the case of a pulse with a

nonuniform transverse intensity profile, the SIT behavior may be described in terms of plane waves interacting independently with dipoles contained in separate coherence volumes throughout the sample. This viewpoint must be corrected for self-focusing and diffraction effects.[1] It applies to optical SIT experiments that involve little or no confinement of the traveling wave by a structure. If propagation occurs in a structure, as in the case of a ring laser,[7] or in our case of microwave waveguide EPR, the SIT behavior depends upon the integrated coupling of dipole sources over the beam cross section. Each source couples with a plane-wave component which sums up with other coupled plane-wave components to contribute to a single waveguide mode. The effect of the mode, therefore, is to alter the form of the plane-wave area[1] theorem of SIT which describes how the pulse area varies with pulse-propagation distance.

Manifestations of the spontaneous zero-area propagation effect[8] in the microwave experiment reported here are of greatest novelty. A weak input pulse, less than $\pi$ in area and shorter than dipole precession damping times, exhibits nearly periodic phase changes of 180° in the carrier wave for increasing distances of propagation. The zero-area pulse which develops is equivalent to a sequence of connected shorter pulses, each of alternating sign in area that sum up toward zero total area. Within a given volume element of the two-level sample, this sequence signifies that dipole transitions alternate between induced absorption and emission, and give rise to reaction microwave fields which alternately subtract from and add to the applied field entering the sample volume element. The field energy in such pulse trains is not degraded according to linear absorption, but is momentarily stored in the sample to some degree, and then reemitted coherently with added time delay in the direction of propagation. The pulse distorts with propagation distance, and for long distances it attenuates at a rate less than that determined by the exponential factor of linear absorption.

## II. EPR MICROWAVE PROPAGATION EQUATIONS

Previous results and theory[1,7] of the optical dipole SIT experiment serve as a basis for microwave SIT analysis. The vector model for SIT is related explicitly to spin $S=\frac{1}{2}$, as in nuclear magnetic resonance. The level splitting is provided by a magnetic field $H_0$, where $\omega_0=\gamma H_0$ is the Larmor frequency, and $\gamma$ is the gyromagnetic ratio. At $x$-band EPR microwave frequencies, a field $H_0\simeq 3\,000$ G provides a total electron-spin polarization $M_0$ in the $x$ direction from a sample of $\alpha,\beta$-bisdiphenylene-$\gamma$-phenyallyl (BDPA) of total free-radical spin density $N=4\times 10^{14}$ cm$^{-3}$. The homogeneous damping lifetime of this free radical is $T_2\approx 0.8$ $\mu$sec, as inferred from echo envelope measurements at 4.2 K, and the inhomogeneous broadening inverse width $T_2^*$ is typically $\approx 0.08$ $\mu$sec, due to nearest-neighbor proton hyperfine interactions. A spin-lattice relaxation time $T_1$ $\simeq 11$ $\mu$sec is obtained from echo measurements. The sample is distributed in powder form down a rectangular waveguide extending in the $z$ direction. Pulse power at 5–10 kW at pulsewidth $t_w\sim 0.15$ $\mu$sec is matched into the guide to excite the $TE_{10}$ mode. In our experiments the sample is distributed in the guide in either of two ways, as shown in Fig. 1. The waveguide mode profile can be accurately determined for a sample geometry in which one-half of the waveguide is filled with free-radical crystals in a matrix of silicon microballons transparent to the microwaves. The filled half extends from $y=\frac{1}{2}d$ to $y=d$, where $d$ is the width of the guide (~1 in.), and the height along $x$ is $\frac{1}{4}$ in. In this configuration the sample is excited in general by elliptically polarized microwave radiation. The magnetic component of radiation is linearly polarized in the $y$ direction near position labeled $\sim\frac{1}{2}d$, circularly polarized near position labeled $\sim\frac{3}{4}d$, and linearly polarized in the $z$ direction at $d$.

Approximate selection of the circularly polarized component of the forward traveling wave is accomplished by placing a thin Teflon tube filled with the sample at position $\sim\frac{3}{4}d$ down the length of the guide. EPR will not occur for the opposite sense of polarization at position $\sim\frac{1}{4}d$. For the Teflon-tube geometry, the guide mode occupied by the sample is difficult to define because of mode distortion caused by a dielectric tube. This mode can be approximated across the tube cross section

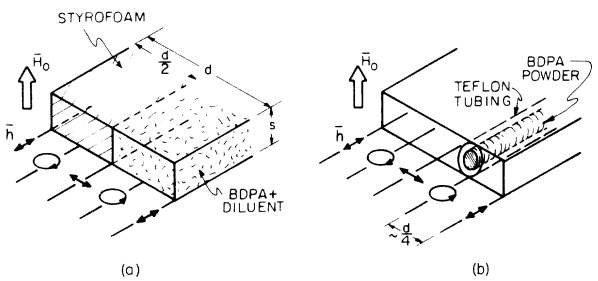


FIG. 1. Waveguide sample geometries. (a) Waveguide half-filled with 18% by volume free-radical powder sample of BDPA distributed in a diluent matrix of silicon microballoons. (b) Sample is in form of BDPA powder inside a 12-gauge thin Teflon tube (approximately $\frac{1}{4}$-in. inner diameter) with axis at position of resonant circularly polarized microwave-field $\vec{h}$.

by a function linear with distance.

The laboratory-frame microwave field at a point $xyz$ in the waveguide, with the waveguide axis along $z$, is defined as

$$\vec{H}_t(z,t) = \hat{\xi}(x,y)h(z,t)\exp\{i[\omega t - k_g z + \varphi(z,t)]\} + \text{c.c.}, \tag{1}$$

where the transverse-mode profile function $\hat{\xi}(x,y)$ is perpendicular to the static magnetic field $H_0$, which is the $x$ direction. Arbitrary phase $\varphi(z,t)$ is defined with possible derivatives $\dot{\varphi}(z,t)$ and $\partial\varphi/\partial z$, which allow for phase modulation during pulse propagation off-resonance.[9] The host medium propagation vector in the waveguide is $k_g = 2\pi/\lambda$; and $\omega$ is the applied microwave frequency. In the slowly varying envelope approximation, $h(z,t)$ in the plane-wave limit is the rotating transverse microwave field defined in a frame of reference rotating at frequency $\omega + \varphi$. According to well-known transformation procedures, the effective field in the rotating frame is given for the plane-wave case ($|\hat{\xi}| = 1$, $\hat{\xi}/|\xi| = \hat{u}_0$) as

$$\vec{H}_{\text{eff}} = \hat{x}_0[H_0 - (\omega + \dot{\varphi})/\gamma] + \hat{u}_0 h(z,t), \tag{2}$$

where $\hat{x}_0$ is the laboratory-frame unit vector along $x$, and $\hat{u}_0$ is the rotating frame unit vector along $h(z,t)$. The Bloch equations[2] in complex form are then

$$dQ/dt = -i\Delta\omega Q + i\beta h_t W - Q/T_2, \tag{3}$$

and

$$dW/dt = \tfrac{1}{2}i\omega_0(Qh_t^* - Q^*h_t) - (W - W_0)/T_1, \tag{4}$$

with the definitions

$$\beta = \gamma^2/\omega_0, \quad h_t = h(z,t)e^{i\varphi},$$

$$Q = (u + iv)e^{i\varphi}, \quad W = -M_z H_0.$$

These equations have been derived and discussed amply in the literature; they apply to electron spin $S = \frac{1}{2}$, with negative gyromagnetic ratio $\gamma_e = -\gamma$. Transverse dispersive and absorptive magnetic polarization components are given by $u$ and $v$, respectively, in the rotating frame. The spin-energy expectation value $W$ may be expressed in terms of the longitudinal equilibrium and nonequilibrium polarization $M_0 = -W_0/H_0$ and $M_z = -W/H_0$, respectively. Transverse and longitudinal relaxation times are $T_2$ and $T_1$, respectively; $\Delta\omega = \Delta\omega_0 + \delta$ and $\Delta\omega_0 = \omega_0 - \omega$; $\omega_0 = \gamma H_0$ is defined at the center of the EPR resonance line (taken to be symmetric in shape); and $\delta$ is the offset frequency away from $\omega_0$ caused by inhomogeneous broadening of the EPR line.

It remains to couple Eq. (3) to Maxwell's equations in the slowly-varying-envelope approximation. In the plane-wave case, the traveling wave equation in the retarded-time frame of reference ($t \to t + \eta z/c$) is written

$$\frac{\partial h_t(z,t)}{\partial z} = -2\pi i k_g \int_{-\infty}^{\infty} d\delta\, g(\delta)Q(\delta,z,t) - \tfrac{1}{2}\sigma h_t(z,t), \tag{5}$$

with a linear scattering term $\sigma$. The normalized inhomogeneous spectral distribution function $g(\delta)$ is applied to sum up the source dipole moments which contribute to the singular self-consistent value of field $h_t(z,t)$.

A consideration of the mode profile function $\hat{\xi}(x,y)$ in Eq. (1) for non-plane-wave conditions requires the usual procedure[10] by which a selected orthogonal mode propagates in the waveguide. As obtained in an earlier treatment,[1] assuming negligible $z$ dependence of $N$ or of $\hat{\xi}(x,y)$, Eq. (5) is modified by a weighted integration of the source terms over the mode profile in the $xy$ plane as follows (see Appendix A):

$$\frac{\partial h_t}{\partial z} = \frac{-2\pi i\eta^2\omega^2}{k_g c^2}\int dx\,dy\,(\hat{\xi}^* \cdot \hat{q}_-)\int d\delta\, g(\delta)Q - \tfrac{1}{2}\pi h_t. \tag{6}$$

The slowly varying rotating field modulus at point $(x,y)$ is now given by $(\hat{\xi}\cdot\hat{q}_+)h(z,t)$, and $\hat{q}_-$ is the complex unit vector (shown in Appendix A) associated with the polarization that rotates in the same direction as the circularly polarized field, where $\hat{q}_\pm = \hat{y} \pm i\hat{z}$. The factor $\hat{\xi}^* \cdot \hat{q}_-$ expresses the projection of radiation from the source term $Q$ at a point $(x,y,z)$ back onto the operating transverse mode. The validity of an assumed invariant mode is discussed in Sec. III. The normalization condition is defined as

$$\iint dz\,dy\,|\xi|^2 = 1, \tag{7}$$

where the integration is taken over the complete mode profile, and the transverse equation

$$\left(\frac{\partial^2}{\partial x^2} + \frac{\partial^2}{\partial y^2} + \gamma_m^2\right)\hat{\xi}(x,y) = 0$$

is satisfied. Therefore,

$$k_g^2 = \eta^2\omega^2/c^2 - \gamma_m^2,$$

where $\eta = \sqrt{\epsilon}$, $\epsilon$ is the host dielectric constant, $\gamma_m$ is the mode eigenvalue, and $c$ is the light speed in vacuum.

## III. EFFECT OF THE TRAVELING-WAVE MODE ON PULSE PROPAGATION

### A. Mode invariance at resonance

One may question whether a particular operating mode remains invariant and uninfluenced by the

dynamic resonance process during pulse propagation, since the mode function $\hat{\xi}(x,y)$ is defined for static nonresonant conditions, where $B=\mu h$ is the transverse microwave field and $\mu=\sqrt{\epsilon}$ is determined by whatever passive dielectric material is present. It is seen that mode constraint is valid during resonance if the condition

$$4\pi M/h \ll 1$$

applies in our experiment. We take

$$B=\mu h(1+4\pi M/\mu h)$$

as a constitutive relation which would possibly distort the mode during resonance, when the transverse magnetization $M$ becomes a function of $h$. Maximum dependence of $M$ on $h$ occurs in the linear regime. In general, for a pulse at resonance, $M\approx M_0\sin\theta$, where $\theta=\gamma h\tau$ for a pulse duration $\tau$. Therefore,

$$\frac{4\pi M}{\mu h}=\frac{4\pi M_0\gamma\tau\sin\theta}{\mu\theta}$$

is a maximum for $\theta\to 0$. For a $\pi$ pulse, we have $\gamma\tau=\pi/h$ for fixed pulse width $\tau$. In our experiment $h$ is of order 1 G. The magnetization $M_0$ is an effective one which is determined by waveguide filling factor and mode profile. Empirically, $M_0$ is best determined in the pessimistic limit by setting the absorption coefficient

$$\alpha=2N_B\pi^2\omega\gamma^2\hbar T_2^*/c\approx 1\,,$$

whereas in the experiment $\alpha$ is smaller by a factor of 10 or more. Now, since

$$M_0=\tfrac{1}{2}\gamma\hbar N_B=\alpha c/4\pi^2\omega\gamma T_2^*$$

is determined, we take rough values of $T_2^*\approx 10^{-7}$ sec for the inverse linewidth of the sample $\gamma=1.7\times 10^7$ rad sec$^{-1}$G$^{-1}$, $h\approx 1$ G, and $\mu\approx 1$. Therefore, $\{4\pi M/\mu h\}_{\max}\approx 0.1$. This ratio is actually of order 0.01 or smaller for the experimental conditions of this investigation ($\alpha<1$); so it can be concluded that the invariant mode profile assumption is valid.

### B. Mode effect on the area theorem

Consider exact resonance excitation ($\Delta\omega_0=\omega_0-\omega=0$) of a symmetric and inhomogeneously broadened line in the absence of phase modulation ($\varphi=0$) and relaxation ($T_2=T_1=\infty$). The experimental condition $T_2>\tau$ favors the assumption of infinite relaxation times. The dependence of pulse area $h\tau\approx\theta/\gamma$ upon propagation distance can be derived for a plane wave from the area theorem[1]

$$d\theta/dz=\pm\tfrac{1}{2}\alpha\sin\theta\,, \tag{8}$$

where

$$\theta=\gamma\int_{-\infty}^{\infty}h(z,t')\,dt'\,. \tag{9}$$

Equation (8) is applicable to an absorber or emitter for $-$ and $+$ signs, respectively. Dipole moments at exact resonance are represented by $\bar{M}_0(\Delta\omega_0=0)$ aligned initially at equilibrium along the $H_0$ field. The perturbing field $h$ tips $\bar{M}_0(\Delta\omega_0=0)$ through an angle $\theta$. If $\bar{M}_0(\Delta\omega_0=0)$ happens to be zero at $t=-\infty$ (the line spectrum has a zero magnetization minimum at its center), then $d\theta/dz=0$ and $\theta_0=\theta=\text{const}$ will be a consequence of Eq. (8). This signifies that the input area $\theta_0$ must remain constant, and the pulse shape must alter in some fashion during propagation to preserve this condition. In a later discussion concerning zero-area ($\theta=0$) pulse propagation, a related effect occurs if the pulse itself acquires a zero Fourier component at $\omega=\omega_0$ in its spectrum. Dipoles at exact resonance are therefore not effectively excited, and anomalous propagation of power takes place over distances exceeding the classical absorption length $\alpha^{-1}$.

The mode profile projection factor $\xi_+=\hat{\xi}\cdot\hat{q}_+$, with $q_+=\hat{y}+i\hat{z}$, is introduced in the Bloch equations by replacing $h_t$ in Eqs. (3) and (4), with $h_t\xi_+$ defined as the local microwave-field amplitude at point $x,y,z$. With $\varphi=0$, and dropping relaxation terms, the Bloch equations are written in component form as

$$du/dt=\Delta\omega v\,, \tag{10}$$

$$dv/dt=-\Delta\omega u+\gamma h\xi_+ W\,, \tag{11}$$

$$dW/dt=-\gamma\xi_+ hv\,. \tag{12}$$

After coupling these equations to Eq. (6) and applying Eq. (9), the area theorem is obtained[1] as

$$\frac{d\theta}{dz}=\pm\frac{\alpha_e}{2}\,\frac{\int_S dA\,(\hat{\xi}^*\cdot\hat{q}_-)\sin(\hat{\xi}\cdot\hat{q}_+\theta)}{\int_S dA\,|\hat{\xi}\cdot\hat{q}_+|^2}-\sigma\frac{\theta}{2}\,, \tag{13}$$

with linear scattering term $\sigma\theta/2$ included. Source dipoles are integrated over the sample region $S$, with $dA=dx\,dy$. The integral over $S$ is introduced in the denominator and is also contained in $\alpha_e$. In the classical limit, $\theta\ll 1$, and therefore the area theorem of Eq. (13) reduces to the linear relation

$$d\theta/dz=\pm\alpha_e\theta-\tfrac{1}{2}\sigma\theta\,. \tag{14}$$

Now Eq. (14) contains the effective absorption coefficient $\alpha_e$ dependent upon the mode profile over the sample. Thus,

$$\alpha_e=\frac{2N\pi\eta^2\omega^2\gamma^2\hbar g(0)}{k_g c^2}\int_S dA\,|\hat{\xi}\cdot\hat{q}_+|^2\,, \tag{15}$$

which reduces to

$$\alpha_0=2N\pi^2\eta\omega\gamma^2\hbar g(0)/c \tag{16}$$

for a plane wave at exact resonance.

Different mode profiles $|\hat{\xi}\cdot\hat{q}_+|$ over the sample will give different forms of the area theorem after integration over the sample region $S$. Consider a mode variation only in the $y$ direction, with no dependence upon $x$, so that $|\hat{\xi}\cdot\hat{q}_+| = \xi(y)$. Independent of how $\xi(y)$ may be described over any region of the guide, the normalization condition, Eq. (7), is applied to the mode function

$$\xi(y) = Cf(y),$$

to give

$$C^2 = \left(\int_0^d f(y)^2\,dy\right)^{-1},$$

with integration limits defined at the guide wall boundaries $y=0$ and $y=d$. Various particular functions $f(y)$ may be assumed to apply between sample boundaries $y_1$ and $y_2$. The integral of the mode modulus over the sample is given by

$$\int_S |\hat{\xi}\cdot\hat{q}_+|^2\,dA = C^2\int_{y_1}^{y_2} f(y)^2\,dy, \tag{17}$$

which is obtained empirically by measuring the effective absorption coefficient $\alpha_e$ in the limit $\theta \ll 1$ from Eq. (14).

### C. Linear mode

The mode function over the sample is approximated by a linear variation. It is convenient for computational purposes to normalize the peak value of $f(y)$ to unity in the sample region by transforming the sample boundary limits from $y=y_1$ and $y_2$ to $y'=0$ and 1, respectively. Therefore we require

$$y = y_1 + (y_2 - y_1)y',$$

and

$$Cf(y) = CC'f(y'),$$

where $C'$ is another constant. The area theorem Eq. (13) now reads

$$\frac{d\theta_m}{dz} = \pm\frac{\alpha_e}{2}\,\frac{\int_0^1 dy' f(y')\sin[f(y')\theta_m]}{\int_0^1 dy' f^2(y')}, \tag{18}$$

where $\theta_m = CC'\theta$ and $\sigma = 0$.

As the simplest example, define $f(y') = y'$. Equation (18) yields

$$\frac{d\theta_m}{dz} = \frac{-3\alpha_e}{2}\left(\frac{\sin\theta_m - \theta_m\cos\theta_m}{\theta_m^2}\right). \tag{19}$$

It is more realistic to define

$$f(y') = a + by', \tag{20}$$

where $a$ and $b$ are constants, for the mode variation over the sample in a thin tube, assumed rectangular in cross section. The modified area theorem [Eq. (18)] becomes

$$\frac{d\theta_m}{dz} = \frac{\pm\alpha_e}{s}\left(\frac{1}{\theta_m}\left[(a+b)\cos(a+b)\theta_m - a\cos a\theta_m\right] - \frac{1}{\theta_m^2}\left[\sin\theta_m(a+b) - \sin a\theta_m\right]\right), \tag{21}$$

where $s = b(a^2 + ab + \frac{1}{3}b^2)$. For $b\to 0$, $d\theta_m/dz$ above reduces to the area theorem for the plane-wave case. For $b=1$ and $a\to 0$, $d\theta_m/dz$ reduces to Eq. (19).

### D. Sinusoidal mode

The sample may be uniformly distributed transversely in the guide over a distance along $y$ between $y=0$ and $y=\frac{1}{2}d$, where

$$f(y) = \sin(2\pi y/d) = \sin\pi y'.$$

Application again of Eq. (18) yields

$$d\theta_m/dz = \pm\alpha_e J_1(\theta_m), \tag{22}$$

where $J_1(\theta_m)$ is the first-order Bessel function. In all cases above, $d\theta_m/dz \Rightarrow \pm(\alpha_e/2)\theta_m$ for $\theta_m \ll 1$.

## IV. PULSE-AREA–PULSE-ENERGY PROPERTIES

Table I lists equilibrium points or areas $\theta_m$ at which $d\theta_m/dz = 0$ for cases: plane-wave SIT [Eq. (8)], linear [Eq. (19)], linear [Eq. (21)], and sinusoidal [Eq. (22)]. Odd points represent those areas at which maximum pulse energy gain occurs for a predominantly inverted system, and even points represent those areas at which minimum pulse energy loss occurs for absorbers mostly in the ground state. The case expressed by Eq. (21) with finite coefficients $a$ and $b$ is intermediate between the plane-wave and linear ($b=1$, $a=0$) cases, and is listed in Table I for $a=1$ and $b=0.3$. The listed sinusoidal case is also of this intermediate character because its equilibrium areas are intermedi-

TABLE I. Equilibrium areas for various propagation modes. Columns "Linear (A)" and "Linear (B)" correspond to cases $b=1$, $a=0$, and $b=0.3$, $a=1$, respectively, applied to Eq. (21).

| Equilibrium point | Plane wave | Linear (A) | Linear (B) | Sinusoidal |
|---|---|---|---|---|
| 1st | $\pi$ | $1.43\pi$ | $1.17\pi$ | $1.22\pi$ |
| 2nd | $2\pi$ | $2.46\pi$ | $2.33\pi$ | $2.23\pi$ |
| 3rd | $3\pi$ | $3.47\pi$ | $3.49\pi$ | $3.23\pi$ |
| 4th | $4\pi$ | $4.48\pi$ | $4.64\pi$ | $4.24\pi$ |
| 5th | $5\pi$ | $5.48\pi$ | $5.73\pi$ | $5.24\pi$ |
| 6th | $6\pi$ | $6.48\pi$ | $6.57\pi$ | $6.24\pi$ |
| 7th | $7\pi$ | $7.49\pi$ | $7.26\pi$ | $7.24\pi$ |
| 8th | $8\pi$ | $8.49\pi$ | $8.29\pi$ | $8.24\pi$ |
| 9th | $9\pi$ | $9.49\pi$ | $9.42\pi$ | $9.25\pi$ |
| 10th | $10\pi$ | $10.49\pi$ | $10.56\pi$ | $10.25\pi$ |
| 11th | $11\pi$ | $11.49\pi$ | $11.69\pi$ | $11.25\pi$ |

ate between those of the plane-wave and linear case of Eq. (19). The successive equilibrium areas differ by essentially $\pi$ for all cases as $n$ increases. For large $n$ the equilibrium area limits are $n\pi$, $(n+\frac{1}{2})\pi$, and $(n+\frac{1}{4})\pi$ for the plane-wave, linear (A), and sinusoidal cases, respectively. For the linear (B) case, equilibrium areas vary about a limiting value of $(n+\delta)\pi$, where $0 \leq \delta \leq \frac{1}{2}$.

For any mode profile other than a plane wave, it is evident that $\theta_m(z)$ cannot converge to an area which characterizes a lossless distortionless pulse, as for the plane-wave $2\pi$ hyperbolic secant pulse. With a field intensity which varies spatially over the sample volume, resonant dipoles are tipped through differing angles $\theta$ such that some dipoles exceed the threshold for SIT, and others do not, giving rise to a net energy loss during pulse propagation. The average tipping angle $\theta_m$ therefore cannot be simply related to the pulse energy as easily as it is related to the absorption and emission process for only those dipoles at exact resonance, expressed by the area theorem. From Eqs. (6), (11), and (12), neglecting linear scattering, pulse energy evolution is described by

$$\frac{d\mathcal{T}}{dz} = \pm\frac{\alpha_e}{W_0 g(0)} \frac{\int_S dA \int dS\, g(\delta)\Delta W(\delta,x,y,z)}{\int_S dA\, \xi^2} , \tag{23}$$

where $\xi$ is taken as real and $\Delta W = W(\delta,x,y,z,t=\infty) - W(\delta,x,y,z,t=-\infty)$ is the energy change of oscillators at frequency $\delta$ after the pulse has subsided. The pulse energy is

$$\mathcal{T}(z) = \frac{\eta c}{4\pi} \int_{\text{over mode}} dA\, \xi^2 \int_{-\infty}^{\infty} dt\, h^2 = \frac{\eta c}{4\pi} \int_{-\infty}^{\infty} h^2\, dt . \tag{24}$$

A pulse-area–pulse-energy argument[1] accounts for deviation from linearity by use of the expression

$$d\mathcal{T}/dz = \pm\alpha_e \mathcal{T} F. \tag{25}$$

The factor $F$ accounts for any nonlinearity, and may be a function of pulse shape, width, area, and mode profile. A useful empirical expression for $F$ under conditions of bell-shaped pulses, $\tau \geq T_2^*$, and $\theta$ not too large ($\lesssim 2\pi$), is given by

$$F = \frac{\int_S dA\,[\xi^2(1-\cos\xi\theta)/\xi^2\theta^2]}{\int_S dA\, \xi^2} . \tag{26}$$

If we define the pulse width $\tau$ as

$$\tau = K(\mathcal{T}/\theta^2)^{-1} \quad \text{or} \quad \theta^2 = (\tau/K)\mathcal{T}, \tag{27}$$

where $K$ is a constant of order unity, then Eq. (25) yields

$$\frac{d\mathcal{T}}{dz} = \frac{\pm\alpha_e \int_S dA\,[1-\cos\xi\theta]}{\int_S \xi^2\, dA} \frac{K}{\tau} .$$

Minimum or maximum energy loss occurs at the condition

$$\frac{d}{d\theta}\left(\frac{d\mathcal{T}}{dz}\right) = 0 = \pm\alpha_e \frac{\int_S dA\, \xi \sin\xi\theta}{\int_S dA\, \xi^2} \frac{K}{\tau} , \tag{28}$$

where the derivative $(d/d\theta)(\tau^{-1}) = 0$ applies in the quasistatic limit that $\theta$ is a constant. The factor multiplying $K/\tau$ above is just the expression for $d\theta/dz$ of the area theorem, Eq. (13), neglecting $\sigma$, which is zero for the condition that areas $\theta$ have attained equilibrium values during propagation. For an absorber, the constancy of $\theta_m$ or $\theta$ cannot remain indefinitely for increasing $z$, although $\theta_m$ may be sustained for some distance with minimum energy loss. The pulse width $\tau(z)$ ultimately increases with increasing $z$, as the pulse loses energy, in order to maintain constant area $[(\text{intensity})^{1/2} \times \tau]$. As $\tau(z)$ approaches $T_2$, the pulse area begins to collapse toward zero.[11] Minimum and maximum energy loss correspond to even and odd equilibrium areas respectively of Table I. Although our phenomenological argument here for the validity of $d\theta_m/dz = 0$ is a limited one, our computer calculations show, in confirmation of experimental results, that this property holds in general for any of the modes which apply.

For experimental calibration purposes, in the limit that the sample is thin, the maximum and minimum electron-spin-echo signals serve as a measure of equilibrium-point areas for a given mode. The sample becomes "thin" simply by shifting the resonance frequency sufficiently far from the carrier frequency to make the sample length $L$ appear small compared to the increased absorption length ($\alpha_e^{-1} \gg L$) at the off-resonance frequency. It is reasonable to assume that the dispersion is approximately flat ($du/d\delta \approx 0$), and therefore negligible under these circumstances. A first weak but sufficiently wide pulse $[\theta_1(0) \ll 1]$ is applied at $t = 0$. A second strong short pulse $\theta_2(T) = \pi$ is applied at $t = T$. The resulting echo amplitude signal at $t = 2T$ will vary in proportion to the echo pulse area $\theta_E(\pi) = \gamma h \tau \ll 1$, or in proportion to the emitted microwave field $h$, since $\tau$ does not change significantly during propagation for small $\theta_E$. This latter condition is necessary for the validity of area theorem analysis[1,12] of the spin echo in the limit $\alpha_e z \ll 1$. As seen from Eq. (8), the weak pulse by itself has the output

$$\theta_1(L) \simeq -\theta_1(0)\alpha_e L/2 ,$$

valid in the linear regime. After a second strong input pulse $\theta_2(T)$ is applied, the spontaneous echo area $\theta_E(2T)$ is evaluated by applying the area theorem and then integrating over the mode profile $\xi$:

$$\theta_E(2T) \simeq \frac{\theta_1(0)\alpha_e L}{2} \frac{\int_S dA\, \xi[1-\cos\xi\theta_2(T)]}{\int_S \xi^2 dA} .$$

The second input pulse area $\theta_2(T)$ is adjusted for extrema in $\theta_E$, namely

$$\frac{d\theta_E}{d\theta_2(T)} = 0 = \int_S dA\, \xi \sin\xi\theta_2(T) ,$$

which is proportional to the generalized area theorem function, Eq. (13) given before, set equal to zero. Thus the condition for defining the equilibrium point areas of the second pulse area is just the condition which gives the echo maxima and minima. The equilibrium point areas listed in Table I may then be calibrated by off-resonance weak echo measurements. Or one may work backwards from a list of a few measured equilibrium echo areas, and estimate a mode profile which fits the measured equilibrium areas.

## V. ZERO-AREA PULSE PROPAGATION

Optical pulse-propagation experiments[5] have demonstrated the effect of imposing a 180° phase shift at the center of a weak pulse ($\theta_0 < 1$) before the pulse enters the resonant medium. The prepared pulse is a zero-area pulse ($\theta_0 = 0$) which enters the medium. For the pulse width condition $\tau \ll T_2$, coherent stimulated absorption during the first half ($\sim\tau/2$) of the pulse is compensated by coherent stimulated emission during the second half ($\sim\tau/2$) for those dipoles at exact resonance ($\Delta\omega_0 = 0$). The 180° phase shift imposes the condition of zero Fourier amplitude of the pulse carrier frequency at $\omega = \omega_0$, and therefore no absorption takes place at exact resonance. Because of the condition $\tau > T_2^*$, the off-resonance dipoles in the inhomogeneous spectrum absorb more energy than they emit. A net absorption therefore takes place, but over distances exceeding many linear absorption lengths $\alpha_0^{-1}$. Output enhancements over normal linear absorption have been observed[5] by as much as a factor of 50 in intensity. Later we will present qualitative experimental observations of this prepared zero-area effect in the microwave EPR case.

We have observed for the first time the spontaneous zero-area propagation effect by EPR pulse propagation in the linear regime. During pulse propagation in the absorbing medium a small finite-area pulse ($\theta_0 < 1$) which enters the medium at $z = 0$ develops a sequence of 180° phase shifts for increasing $z$ until a final zero-area $\theta(z) = 0$ is established. For this to occur, the pulse width $\tau$ for all $z$ must obey the condition

$$\frac{1}{\tau} \gtrsim \frac{1}{T_2^*} + \frac{1}{T_2} .$$

This allows the entire two-level distribution to respond coherently in some degree towards the limit of sharp line response. We assume $T_2 \to \infty$, and consider the particular case $\tau \sim T_2^*$ which applies in our experiment.

Crisp[8] has presented an analytic treatment of spontaneous linear zero-area pulse propagation by considering an input pulse of the general form

$$h(0,t) = h_0(t/\tau)^n e^{-t/\tau} .$$

The integer $n$ is chosen to best fit the input experimental pulse shape. A Fourier analysis with the condition $W \approx W_0$ in the weak excitation limit gives

$$h(z,t) \equiv n!\, e^{-t/T_2^*} \left(\frac{1}{\alpha_e}\right)^{n/2} \frac{1}{\tau^n} J_n\left(2\left(\frac{t}{T_2^*}\alpha_e z\right)^{1/2}\right) , \tag{29}$$

where $J_n$ is the $n$th-order Bessel function, and we chose $T_2^* \simeq \tau$. We extend the energy analysis of Crisp to the case $n = 1$ in Appendix B, which is more representative of a real pulse, and obtain the spontaneous zero-area energy

$$\mathcal{T}_1(z) = \frac{\eta c}{4\pi} \int_{-\infty}^{\infty} h_{n=1}(z,t)^2\, dt$$
$$= \mathcal{T}_1(0) e^{-\alpha_e z/2}[I_0(\tfrac{1}{2}\alpha_e z) - I_1(\tfrac{1}{2}\alpha_e z)] ,$$

where $I_0$ and $I_1$ correspond to zero and first Bessel functions with imaginary arguments. For large $z$ where $\alpha_e z > 1$, the asymptotic energy for any $n$ is

$$\mathcal{T}_n(z) \sim (1/\alpha_e z)^{n+1/2} .$$

## VI. OFF-RESONANCE PULSE-PROPAGATION FREQUENCY SHIFT

Pulse-propagation off-resonance in a two-level system must take into consideration the time and spatial derivatives of $\varphi(z,t)$ introduced in Eq. (1). In the case of an absorber with inhomogeneous broadening ($T_2 \gg T_2^*$) in the linear regime ($\theta \ll 1$) with $W \approx W_0$, a previous treatment[9] yields the equation

$$\frac{d\langle\dot\varphi\rangle}{dz} = \frac{\alpha_e W_0}{2\pi g(0)\mathcal{T}} \int d\delta\, g(\delta) |\tilde h(z,\delta)|^2 (\Delta\omega - \langle\dot\varphi\rangle) . \tag{30}$$

Now $\alpha_e$ takes into account the waveguide mode. The average frequency shift is defined by

$$\langle\dot\varphi(z)\rangle = \frac{\int_{-\infty}^{\infty} \dot\varphi h^2(z,t)\, dt}{\int_{-\infty}^{\infty} h^2(z,t)\, dt} ,$$

and the pulse Fourier transform is given by

$$\tilde h(z,\delta) = \int_{-\infty}^{\infty} h e^{-i\varphi} e^{i\Delta\omega t}\, dt ,$$

noting that $\Delta\omega = \Delta\omega_0 + \delta$. Let the pulse $h(0,t)$,

applied off-resonance by amount $\Delta\omega_0$, be described in terms of its intensity

$$|\tilde{h}(0,\delta)|^2 = (\theta^2/\gamma^2)\exp[-(\Delta\omega_0+\delta)^2\tau^2],$$

and express the EPR line shape by the Gaussian distribution

$$g(\delta) = (T_2^*/\sqrt{\pi})\exp(-\delta^2 T_2^{*2}).$$

The frequency-shift relation reduces to

$$\frac{d\langle\dot{\varphi}\rangle}{dz} = 2\alpha_e s^3(\Delta\omega_0\tau)\exp[-(\Delta\omega_0\tau s)^2], \tag{31}$$

valid for $\langle\dot{\varphi}\rangle \ll \Delta\omega_0$ and $\alpha_e z \ll 1$, where

$$s = T_2^{*2}/(\tau^2 + T_2^{*2}).$$

The maximum frequency shift occurs at

$$\Delta\omega_0|_{\max} = 1/\sqrt{2}s\tau,$$

and

$$\left.\frac{d\langle\dot{\varphi}\rangle}{dz}\right|_{\max} = -\sqrt{2}\alpha_e s^2 e^{-1/2}. \tag{32}$$

The frequency behavior in the nonlinear regime, where $W \neq W_0$, cannot be treated by the above relations. Investigation[9] by computer simulation for off-resonance hyperbolic-secant-shaped pulses show that the frequency shift for small $z$ may be obtained from the empirical relation

$$\left.\frac{d\langle\dot{\varphi}\rangle}{dz}\right|_{z\simeq 0} = 2\left.\frac{d\langle\varphi\rangle}{dz}\right|_{\text{linear}}\left(\frac{1-\cos\theta}{\theta^2}\right), \tag{33}$$

where $d\langle\dot{\varphi}\rangle/dz|_{\text{linear}}$ is given by (30). This relation shows that the frequency shift is maximum for small areas ($\theta \to 0$), nearly disappears for even multiples of $\pi$, and revives for odd multiples of $\pi$. Although the microwave pulses in our experiment are not literally of hyperbolic-secant-shaped character, any bell-shaped pulse with the above areas displays a very similar behavior.

At liquid-nitrogen and room temperatures, the BDPA sample line is primarily exchange narrowed, corresponding to a homogeneous damping time $T_1 \simeq T_2 \sim 0.1$ $\mu$sec. In this limit the effect is to produce frequency shifts opposite to the inhomogeneous broadening case above. We will not present this second case here. The number of off-resonance absorption lengths necessary to see a significant shift in this limit proved to be too small in our experiment because of the reduced Boltzman factor.

## VII. THE MICROWAVE PULSE PROPAGATION EXPERIMENT–APPARATUS AND PARAMETERS

The block diagram of the pulsed EPR system is shown in Fig. 2. A tuneable $x$-band high-power pulsed magnetron (2J51) served as a source of microwave pulses which were controlled in intensity and spectral width by adjustable attenuators and filters. A section of spiral waveguide to contain the sample was specially constructed in close-packed helical shape to fit between the pole pieces of a 12-in. magnet. After microwave detection, the output pulse from the sample was observed in the time domain on a fast oscilloscope, or observed in the frequency domain by use of a microwave spectrum analyzer. A microwave ferrite isolater following the attenuators served to prevent feedback reflections. A fraction of the input signal was shunted for monitoring of input power and pulse shape.

The helical waveguide indicated in Fig. 2 is 1 $\times \frac{1}{4}$ in. rectangular I.D., made of soft copper, and is designed to propagate the $TE_{10}$ mode. A spiral of $2\frac{1}{2}$ turns provides a sample path lenth of ~100 cm. Tapered input and output ends of the guide match impedance into standard waveguide sections, connected in turn to pulse source and detectors. For the Teflon tube and half-filled guide sample geometries, the static field $H_0$ at 3 kG did not have a spatial variation over the spiral guide length that exceeded more than ~1 G. The field inhomogeneity at any given point in the sample was of the order 0.05 G/mm. A thermocouple monitored the temperature of the guide helix.

By means of an isolator and mechanical switch, one could observe the transmitted pulse or reflected pulse, if any could be measured of the latter, by the same detector system. A Polarad

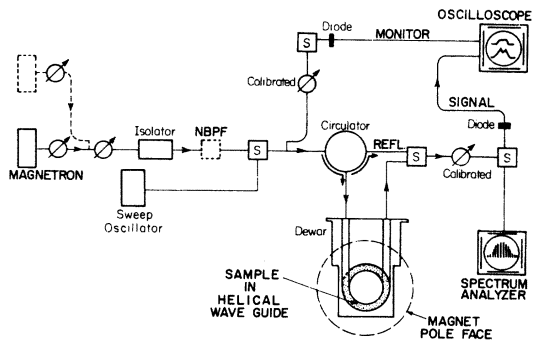


FIG. 2. Block diagram of pulsed EPR microwave apparatus. The pulse signal output or the reflected signal out of the input end of the helical guide (transmitted through the circulator) is selected for observation in the time (oscilloscope) or frequency (spectrum analyzer) domain by switches S. Single pulses derive from a magnetron with a second magnetron available for spin-echo observations from closely spaced pulse pairs. A narrow-bandpass filter NBPF provides a pulse spectrum narrower than the magnetron output spectrum. Other switches S allow a sweep oscillator reference signal to be connected for calibration purposes. Circle symbols with arrows designate variable attenuators.

TSA-W spectrum analyzer sampled output pulse spectra at 15 pulse/sec repetition rate,[5] corresponding to a period far in excess of the $T_1 \approx 11$ $\mu$sec relaxation time of the BDPA sample at 4.2 K. The absolute resolution of spectrum analyzer was better than 1/10 MHz.

Long sample lengths $L$ were required for the condition $\alpha_e L > 1$ to apply so that SIT could cause significant changes in the output pulse shape and delay relative to the input pulse. In order to satisfy the slowly-varying-envelope condition $\alpha_e \lambda < 1$ also, given that $\lambda \simeq 4$ cm at $x$-band frequency, we have chosen $L \sim 100$ cm to give $\alpha_e L \sim 5$ and $\alpha_e \lambda \simeq \frac{1}{5}$. The accuracy of our measurements does not distinguish between the extreme inequality $\alpha_e \lambda \ll 1$, which applies at optical wavelengths, and the weaker inequality $\alpha_e \lambda < 1$. Higher-order corrections to the theory because of the weaker inequality do not make a significant difference in the overall predictions of SIT.

The free-radical BDPA sample is primarily inhomogeneously broadened at 4.2 K because of electron-proton hyperfine interactions.[13] This provides an inverse linewidth $T_2^* \sim 0.1$ $\mu$sec compared with a longer homogeneous relaxation time $T_2 \simeq 0.8$ $\mu$sec, and a $T_1 = 11$ $\mu$sec. Line-shape experiments show a BDPA spectrum which is slightly asymmetric, caused possibly by a residual antiferromagnetism.[14] This small asymmetry does not significantly effect our SIT measurements, but it does show up in terms of a small asymmetry in the final output pulse spectrum. We assume a symmetric two-level spectrum in our analysis. At room and liquid-nitrogen temperatures, the BDPA sample gives $T_1 = T_2 \sim 0.1$ $\mu$sec, because of electron exchange narrowing. This time is too short to enable SIT observations with our available input pulse widths. At higher temperatures exceeding 10 K, the values of $\alpha_e L$ were too small to allow observations of SIT.

#### Waveguide-sample transmission parameters

For the tube sample geometry, clear 12-gauge Teflon tubing was filled with BDPA powder. The composite dielectric constant of this combination was determined from frequency-shift measurements in a specially prepared cavity. For the tube axis located at $\sim\frac{3}{4}d$ from the guide wall, the experimental constants are $\omega/c = 2$, $\eta^2 = 2$, $k_g = 1.6$, and $\alpha_e^{-1} = 20$ cm. Because of the differing sample dielectric constant, this value of $k_g$ results from a self-consistent mode calculation[15] in which three different transverse rectangular regions are assumed and matched by the appropriate boundary conditions. Similar dielectric measurements were made for the half-filled guide geometry. A unique $TE_{10}$ mode character prevails along the transverse guide $y$ direction even in the presence of changes in the medium dielectric constant. Half of the rectangular guide from $y = 0$ to $y = \frac{1}{2}d$ was filled with a styrofoam spacer, and the other half from $y = \frac{1}{2}d$ to $y = d$ contained a homogeneous mixture of 18% powdered BDPA by volume mixed with inert silicon microballons (hollow silicon spheres). This percentage mixture on the low side insured that the mode constraint remained valid at resonance, as discussed in Sec. III. The experimental constants for the half-filled guide geometry are $\omega/c = 2$, $\eta^2 = 1.3$, $k_g = 1.65$, and $\alpha_e^{-1} = 25$ cm$^{-1}$.

In order to be certain that the EPR pulse propagation effects were not to be confused with spurious signal background effects, it was important to assess background losses, scattering, and reflections. As mentioned previously, the mechanical switch (Fig. 2) enabled the measurement of transmitted and reflected signals, which could be compared to the input pulse as well. The small signal cw characteristics of the entire system were measured by use of a microwave sweep oscillator (HP 686C) over a controlled range of frequencies. Reflections amounting to about 4%–10% of signal input varied somewhat as a function of frequency. The best experimental measurements were made at those frequencies in the range of 9.3–9.7 GHz where the reflections were minimized to approximately 4% of the input pulse itself. The data were taken in terms of relative signal measurements. Detector nonlinearity was taken into account by taking readings from calibrated attenuators which brought measured signal outputs up to the same oscilloscope amplitude as the input. Amplitude differences were read from the attenuator in terms of db. All db measurement errors were within $\pm\frac{1}{3}$ db or 4%.

Low-loss tapered guides were used for impedance matching into and out of the sample spiral guide. These tapers produced less than $\frac{1}{3}$ db attenuation compared to a straight guide of the same length, and virtually no reflections were caused by the tapers. With the sample included in the helix, background attenuation (for an off-resonance signal) amounted to 2 db, and a 5–15 db reflection signal was seen relative to the desired transmitted signal. Overall attenuation losses implied a background scattering loss corresponding to $\sigma^{-1} = 250$ cm at room temperature. At 4.2 K, this parameter decreased to $\sigma^{-1} \simeq 500$ cm. Acid cleaning of the copper helix decreased the losses even further to $\sigma^{-1} > 800$ cm.

For the two sample geometries, the absorption coefficient $\alpha_e$ for $H_0$ applied in the "resonant direction" was compared to the measured $\alpha_e$ for the reversed antiresonant field direction $-H_0$. In the case of the tube sample, presumed to be all lo-

cated ideally only at the position for pure circularly polarized microwaves, the ratio would theoretically be infinity. Because of sample extension along $y$, the experimentally determined ratio was found to be a maximum of 25, with lesser values due to error in tube positioning. With the half-filled guide geometry, a ratio of $4.1 \pm 0.6$ was computed based upon the measured dielectric constants of the guide media. This ratio compared very well with the measured value of $4.3 \pm 0.2$, which confirmed the mode description of the particular geometry.

## VIII. EXPERIMENTAL RESULTS

### A. Mode modification of SIT

Figures 3 and 4 show output pulses in the time domain for a BDPA sample in the Teflon tubing configuration, with sample length $L = 90$ cm corresponding to $\alpha_e L = 5.5 \pm 0.3$. The more complex output pulse shapes of Fig. 3 result from the steeper rising and falling input pulse shown which is unfiltered, injected directly from the magnetron. A smoother bell-shaped input pulse in Fig. 4 is obtained out of a filter of bandwidth ~ 8 MHz.

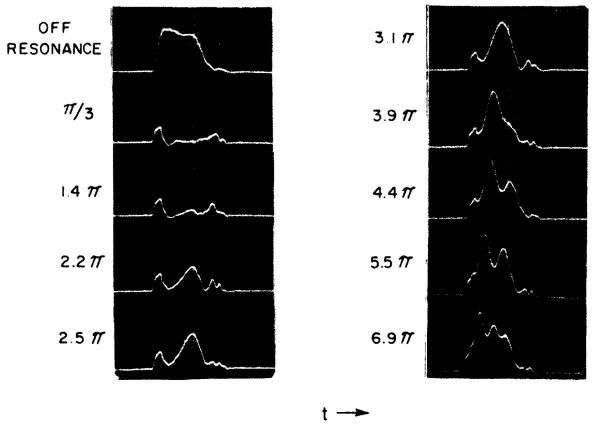


FIG. 3. Nonlinear output pulses at exact resonance ($\Delta\omega_0 = 0$) in the time domain (0.05 μsec/div) for the tube waveguide geometry with $\alpha_e L \approx 5.5$. Vertical output signals from the diode (Fig. 2) are proportional to $h(L, t)$, which determine $\theta$, and are labeled by input areas $\theta_0$, from which $\theta$ evolves. All $\theta_0$ obtain from the input pulse shape $h(0, t)$ shown at the top left. All output signals $h(L, t)$ obtain from input signals $h(0, t)$ adjusted to the same amplitude on the oscilloscope. Multiple-pulse break-up characteristic of SIT appears for the highest input areas. With no NBPF (Fig. 2), ragged pulse edges in the output are caused mostly by nonresonant spectral wings, frequency modulation in the magnetron pulse input, and deviation from exact sample resonance because of $H_0$ spatial variations over the helix geometry.

This gives rise to correspondingly smoother looking output pulses shapes, but with less maximum output in total area available because of less power by a factor 2 contained in the filtered input pulse. The definition of pulse area $\theta$ [Eq. (9)] and the pulse envelope transform defined in Eq. (30) are identical except for a constant factor, when $\varphi = \Delta\omega = 0$. The amplitude at the center of the pulse spectrum $\tilde{h}(z, 0)$ is therefore proportional to the pulse area. A plot of pulse area output versus input pulse power, in terms of db attenuation readings, is shown in Fig. 5 for the data from Fig. 3. The appearance of pulse breakup characteristic of SIT is evident. The maxima and minima of Fig. 5 correspond to the equilibrium point areas at which minimum and maximum pulse energy loss take place. The mode shape which gives these maxima and minima is taken to be

$$f(y) = 1 - 0.3y. \tag{34}$$

This 30% linear mode assumes a rectangular rather than circular sample cross section, and applying this mode together with experimental parameters $T_2 = 6\tau$ and $2\pi/T_2 = 0.7\delta_A$, where $\delta_A$ is the spectral resonance linewidth (all defined at full width half maximum), gives the computer plot pulse shapes of Fig. 6. These shapes apply to the data of Fig. 3, for the unfiltered input pulse. Good correspondence is obtained in the time plots between the experimental and computer results, with some discrepancy near $2\pi$. On the other hand, the computer

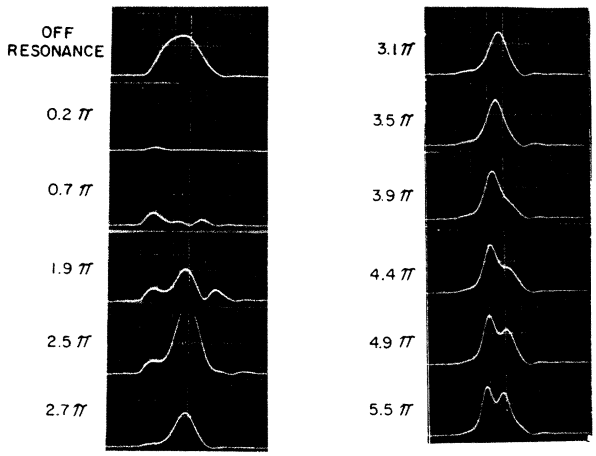


FIG. 4. Nonlinear output pulses with narrow-band pass filter (NBPF, Fig. 2) switched in. The conditions otherwise are the same as in Fig. 3 except for a different sequence of input areas $\theta_0$. SIT characteristics are seen as in Fig. 3 with pulse symmetrization more evident. Signals corresponding to $\theta_0 = 0.7\pi$, $1.9\pi$, and $2.5\pi$ are multiplied by a gain factor 2.8 relative to the remaining normalized signals.

plot prediction for $\theta_{out}/\theta_{in}$ vs $\theta_{in}$ shown in Fig. 5 does not correspond in shape to the experimental plot. The sensitivity of $\theta_{out}$ predictions to nonideal experimental conditions is more critical than are pulse shape predictions. The computer simulation does not take into account pulse carrier frequency modulation and the variation from exact resonance ($\Delta\omega_0 = 0$) at positions $0 \leq z \leq L$ in the sample helix waveguide (because of static $H_0$ field spatial variations). Although $\alpha_e$ may be assigned an average value for low pulse intensities, it does not apply in the regime of nonlinear propagation when $\alpha_e$ is actually some function of $z$. Indeed, the $H_0$ variations were of order one gauss over the helix, which corresponds to about a 3-MHz off-resonance shift at points in the helix, but spanned somewhat by a wider pulse spectrum. Nevertheless, one notes in the computer plot of Fig. 5 that values of $\theta_{in}$ at $\theta_{out}/\theta_{in} = 1$, which are the equilibrium points of column (B) in Table I, do relate to the experimental curve, explained in the caption. We note in particular that those regions (around the unstable equilibrium points) in which experiment yields $\theta_{out}/\theta_{in} < 1$, instead of $\theta_{out}/\theta_{in} > 1$, are just the regions where computer predicted large pulse widths and pulse delays would be inhibited by frequency modulation and spatial variation of $H_0$ over the helix.

Designated input areas in experimental plots were determined by spin-echo measurements and

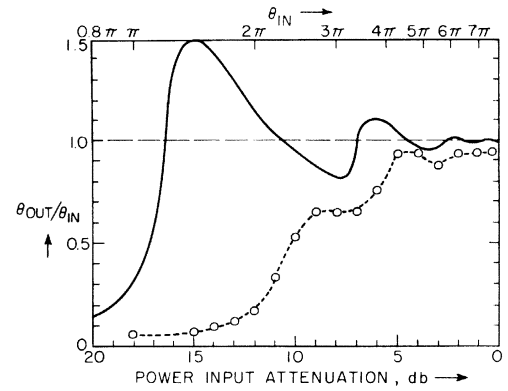


FIG. 5. Pulse-area-output–pulse-area-input ratio $\theta_{out}/\theta_{in} = \theta(L)/\theta_0$ vs $\theta_{in}$ (top) and power input (bottom, relative to maximum power at 0 db). The dotted curve shows experimental results from data and conditions represented by Fig. 3, approximated by the mode shape function of Eq. (34). With this function the solid-line computer plot shows $\theta_{out}/\theta_{in} > 1$ in regions of $\theta_{in}$, not evident from the experiment (see text). Unstable and stable equilibrium areas occur respectively at odd and even points listed in Table I under "Linear (B)" column. These points conform approximately to $\theta_{in}$ at the beginning and end of each rise in the experimental curve, where $\theta_{out}/\theta_{in} = 1$ intersections occur in the computer plot.

computer analysis. Application is made of the spin-echo maxima and minima condition discussed in Sec. IV. For a plane wave, a $\theta_2 = 2\pi$ pulse would produce a zero-amplitude first minimum. For an assumed linear mode given by (34), the first echo maximum and minimum would occur at $\theta_2 = 1.4\pi$ and $2.4\pi$, respectively. It was found that the first maximum spin echo occurred for a pulse attenuated $16 \pm 0.5$ db below the maximum input power (with no filter). By computer simulation fit of the pulse shape, this pulse corresponded to an area $\theta_2 = 1.2\pi \pm 0.1\pi$, near that expected for a linear mode variation of 30% chosen in Eq. (34). The equilibrium point areas at which maxima and minima appear in Fig. 5 are therefore intermediate between the case of 100% variation and plane-wave mode, listed in Table I.

The ideal $2\pi$ hyperbolic-secant shape is not predicted to be the analytic final pulse shape during propagation for any mode other than plane wave. We note, however, from Fig. 7 that the spectral shape for certain larger area pulses, such as $\theta = 2.8\pi$, corresponds to exponential asymptotic fall off at $\Delta\omega = \pm\infty$. Since the Fourier transform of a hyperbolic-secant pulse is also a hyperbolic-secant function, we see, therfore, a tendency for pulses, even in the nonplane regime, to evolve toward a hyperbolic-secant character.

Figure 8 shows the signal output for the half-filled waveguide geometry, with 4.5 absorption lengths of sample BDPA. Longer pulse lengths were employed to achieve multiple-pulse break-up.

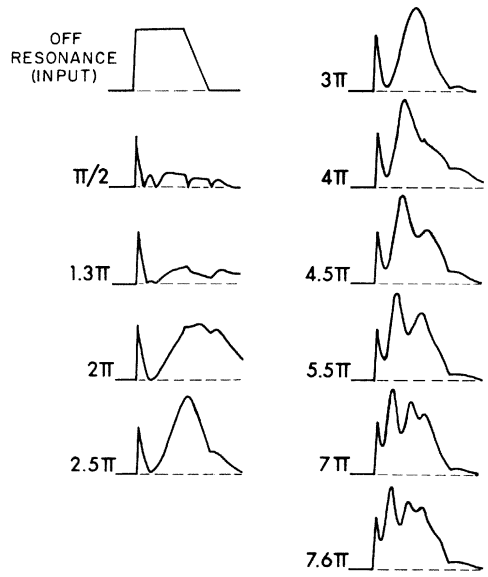


FIG. 6. Computer plot of time-domain [$h(L,t)$ from Eq. (6)] pulse shapes corresponding to the data and conditions represented by Fig. 3. Plots are approximately to within 10% of actual pulse shapes, with inputs approximated by straight-line contours shown upper left.

The mode structure is responsible for washing out the last few peaks in the break-up oscillations. This cannot be attributed to loss of phase memory associated with $T_2 \sim 0.8$ $\mu$sec, which is not short enough to account for the observed damping.

### B. Zero-area pulse propagation

If the wings of the pulse spectrum fall well within the spectrum of the spins ($T_2^* \ll \tau$), the pulse spectrum amplitude $\tilde{h}(z, \Delta\omega)$ is essentially uniformly attenuated for small $\theta$ over all frequencies $\Delta\omega$ in the pulse. When the pulse spectral width $1/\tau$ is comparable or greater than the absorption linewidth $\sim 1/T_2^*$ (since $T_2 \gg T_2^*$), a hole centered at $\Delta\omega_0 = 0$ is observed to be burned out of the pulse spectrum, as shown in Fig. 9. The hole width corresponds approximately to $1/T_2^*$, with a cusp-like indentation at $\Delta\omega_0 = 0$. If we assume the asymptotic Bessel function description given by Eq. (29) for $n = 1$, the sides of the hole have a slope $|\tilde{h}(0)(T_2^*/\alpha_e L)|$. This behavior is obtained from the ideal picture of a spontaneous zero-area propagation model, pointed out later. The hole generated here should not be mistaken as simply one which occurs because the profile of the spin spectrum is eaten out of the pulse spectrum by the usual linear absorption process. In fact, the more subtle zero-area effect serves to label the propagation as leading to SIT itself in situations where $T_2^* \geq \tau$.

Consider the output pulses shown in Figs. 10 and 11 for the Teflon tube configuration. In Fig. 11 the spectral hole in the small-$\theta$ pulse region begins to fill up for increasing $\theta$, and at $\theta \sim 2\pi$ the pulse shape spectrum has become essentially bell shaped. The hole filling process implies unequivocally that *energy is being returned to the two-level system coherently*, a mark of the SIT process. Pulses at $\theta \geq 2\pi$ form without spectral holes and are predominantly energy conserving as they propagate. Demonstration of this spectral behavior in optical experiments has so far not been achieved. The combined nonlinear effects of anomalous pulse delay, pulse intensity output, and pulse break-up are taken as evidence of the SIT

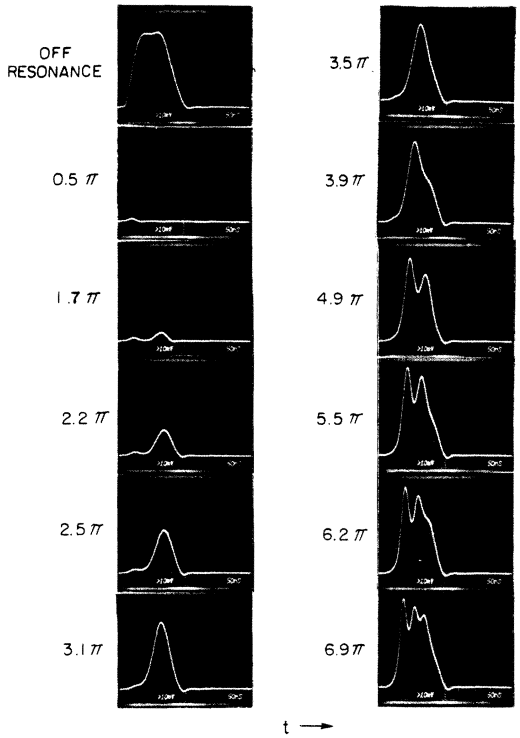


FIG. 8. Nonlinear output pulses in the time domain for the half-filled waveguide geometry with $\alpha_e L = 4.5$. Conditions otherwise are similar to those of Fig. 4, with pulse break-up evident.

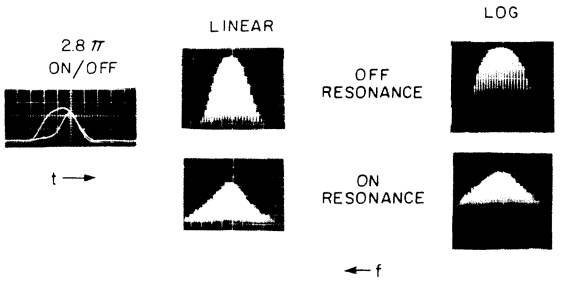


FIG. 7. Spectral pulse shape of output vs input pulse. At left the pulse shape on- and off-resonance (0.05 $\mu$sec/div) shows the on-resonance pulse symmetrized and shorter than the superimposed off-resonance pulse. The Gaussian character of the input (off-resonance) pulse is altered toward the Lorentzian character of the on-resonance pulse. These pulses show spectral amplitudes in the wings proportional to $e^{-t}$ (linear) and $t$ (log), respectively.

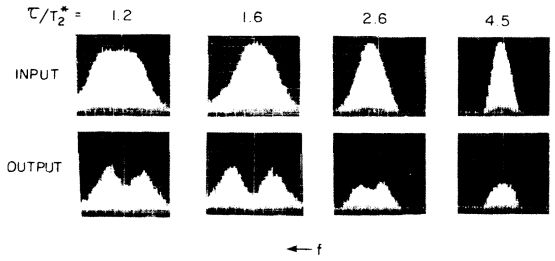


FIG. 9. Input and output weak-pulse spectra compared for various ratios of pulse width to inverse spin spectrum width ($\tau/T_2^*$). For increasing $\tau/T_2^*$ the change from spontaneous zero-area regime to the Beer's-law regime occurs. (Corresponding time-domain plots are shown later in Fig. 16.) $\alpha_e L = 2.2$ for all signals.

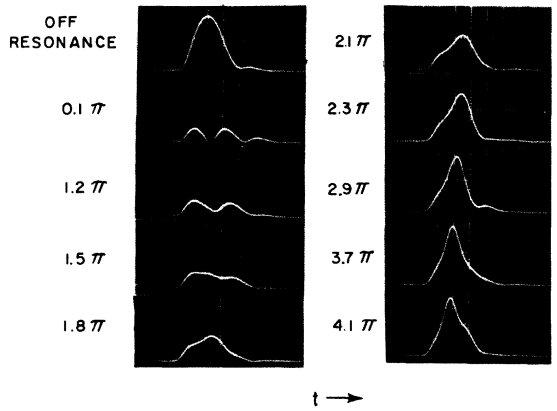


FIG. 10. Nonlinear output pulse shapes in the time domain, identical to conditions of Fig. 4, except that $\tau \approx T_2^*$ here. Spontaneous zero-area pulse oscillations are evident for $\theta_0 = 0.1\pi$ and $1.2\pi$.

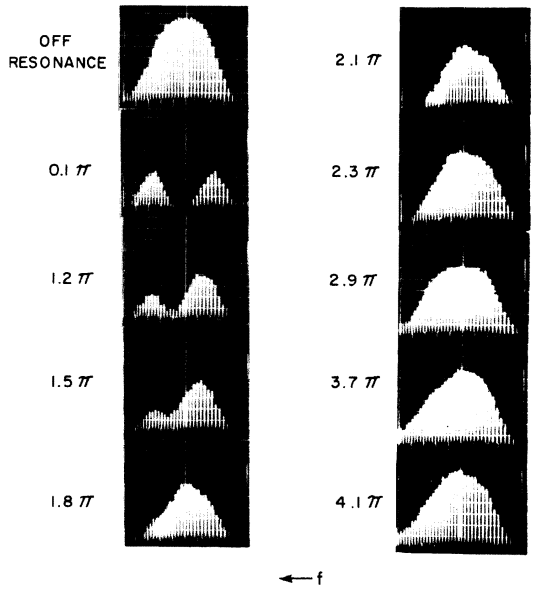


FIG. 11. Corresponding pulse Fourier spectra of Fig. 10 pulse time domain pulse shapes (20 MHz full scale). For small $\theta_0$, the hole filling of the spectrum at $\Delta\omega_0 \sim 0$ indicates spontaneous zero-area pulse disappearance as SIT develops for increasing $\theta_0$. Frequency shift in the dip of the spectrum is caused by effects of magnetron frequency modulation and slight asymmetry in BDPA spin-resonance line shape.

effect on optical experiments. Each of these properties alone is not free of ambiguity of coincidence with other propagation effects, whereas the spectral hole filling property is indeed a unique signature of the onset of SIT shown here.

The spontaneous reversal from an absorption to an emission condition is shown schematically in Fig. 12. Such reversals build up in succession over long propagation distances as indicated in the next schematic Fig. 13. Figures 14 and 15

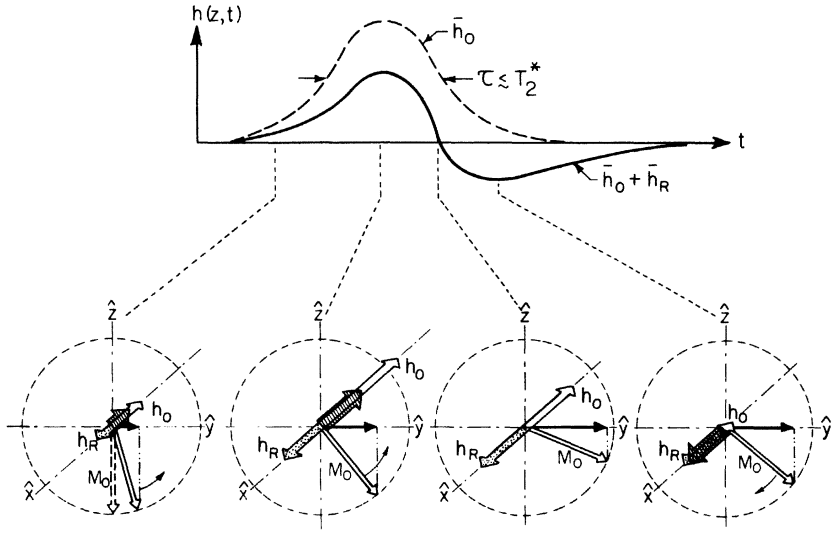


FIG. 12. Vector representation of the spontaneous zero-area pulse propagation effect at exact resonance. In a thin sample the pulse $\vec{h}_0$ is applied for short $\tau \leq T^*$, and tips the equilibrium $M_0$ from the $-z$ direction. As $\vec{h}_0$ increases, reaction field $\vec{h}_R$ (dotted arrow along $x$) opposes $\vec{h}_0$ (white arrow along $x$) during absorption, where $h_R$ is proportional to source dipole vector (black arrow along $y$) component. When the applied $\vec{h}_0$ decreases, $\vec{h}_R$ exceeds $\vec{h}_0$, and coherent emission returns the vector $\vec{M}_0$ toward the ground state. The resultant field $\vec{h}_0 + \vec{h}_R$ exhibits a 180° phase shift as absorption shifts to emission, with the emission actually much weaker for the thin sample case shown. The pulse area is not zero for $z < \alpha_e^{-1}$.

show, respectively, the accumulation of absorption-emission cycle oscillations, displayed respectively in the time and frequency domain for a fixed sample length $L$ corresponding to $\alpha_e L = 5$ at 4 K. By increasing the temperature of the sample, $\alpha_e$ is correspondingly decreased, and $\alpha_e L$ is varied. The effect of approach to zero area in Fig. 15 is seen for increasing $\alpha_e L$ as a buildup of the spectral hole in the pulse. The corresponding time domain display of the approach to zero area is shown in Fig. 14, where the signals are heterodyned with a weak reference microwave oscillator. The alternation in the sign of the heterodyne beat signal shows that the absorbed and emitted radiation signal lobes are 180° out of phase. These lobes signify that the $v$ polarization creates a reaction field which alternately subtracts (absorption) and then adds (emission) to the imagined applied field at a particular volume element in the sample. By varying the pulse width $\tau$, keeping $\alpha_e L$ constant, Figs. 9 and 16 show the transition from exponential absorption to the alternation of absorption and emission in the limit that $\tau \lesssim T_2^*$. In all of these cases, the anomalous propagation of pulse energy over distances exceeding $\alpha_e^{-1}$ takes place as $\tau/T_2^* \to 0$.

In Figs. 17, a comparison of signal output is shown between small finite-area input pulses and artificial zero-area constructed input pulses. A single pulse is delayed 180° or 0° with respect to a source pulse from which it is derived, and then the two pulses are injected into the sample in sequence. The comparison of outputs (a) single pulse, (b) zero-area double pulse (180° out of phase), and (c) finite-area double pulse (in phase), shows that anomalous propagation for the case (b) is greater than in (c) by about a factor of 2 in power.

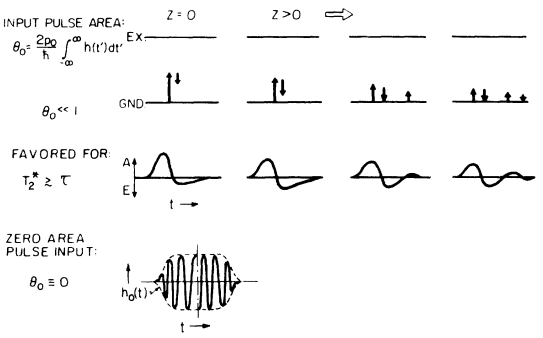


FIG. 13. Absorption and emission during spontaneous zero-area pulse propagation. The signal evolution shown in Fig. 12 builds up as successive volume elements are excited during propagation, and $\theta$ evolves toward zero for increasing $z$. At exact resonance coherent absorption is balanced by coherent emission alternately, but propagation is not completely lossless because of net absorption due to off-resonance transitions. The Fourier spectrum of the output pulse is similar to that of an artificially created zero-area pulse (bottom signal with carrier 180° phase shift at pulse center).

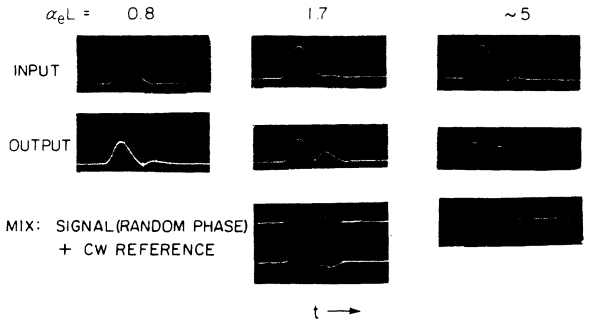


FIG. 14. Approach of propagating pulse toward a spontaneous zero-area pulse in the time domain (0.05 μsec/div) for $\tau/T_2^* \approx \frac{1}{3}$. For larger absorption lengths $\alpha_e L$, the buildup of zero-area oscillations occurs. Input and output pulse shapes are compared. For $\alpha_e L = 1.7$ and 5, a constant reference signal mixed with the output pulse shows interference at random phase with respect to the output pulse indicating 180° phase shifts between absorption and emission portions of the pulse.

### C. Off-resonance pulse carrier frequency evolution

The parameters of the microwave EPR experiment allow a clear measurement of pulse carrier "frequency pushing" for pulses applied off-resonance by amount $\pm \Delta\omega_0$. Frequency pushing implies that $d\langle\dot{\varphi}\rangle/dz$ of Eq. (30) for an absorber is negative

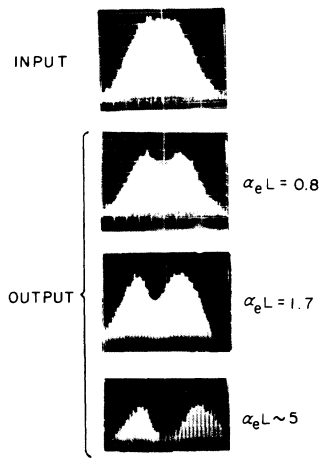


FIG. 15. Spectral behavior of spontaneous zero-area pulse propagation (20 MHz full scale). Corresponding to Fig. 14, the output pulse spectra develop a deeper cusp at $\Delta\omega_0 \approx 0$ for increasing $\alpha_e L$.

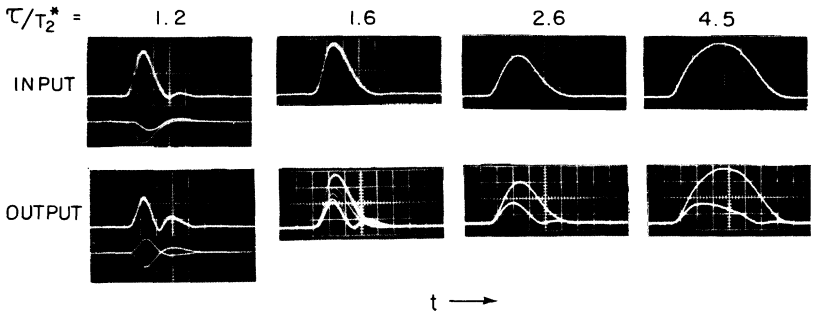


FIG. 16. Change of output pulse in time domain (0.05 μsec/div) from spontaneous zero area to classical absorption, as $\tau/T_2^*$ is increased. These spectral outputs correspond to the time-domain outputs of Fig. 9.

for $\omega < \omega_0$ and positive for $\omega > \omega_0$; namely $\omega + \langle\dot{\varphi}\rangle$ moves away from $\omega_0$ according to Eq. (31), presuming that $\langle\dot{\varphi}(z)\rangle \ll |\Delta\omega_0|$ for all $z$. This behavior is a consequence of the inhomogeneously broadened absorbing wings of the spin resonance line which absorb Fourier components from the pulse spectrum wing portion toward the line center. This effect, although linear in the regime given by Eq. (31), becomes nonlinear for intense pulses that require a more general solution of Eq. (30). Effects of homogeneous broadening were not significant at 4.2 K, where the inhomogeneous hyperfine EPR linewidth is dominant. At higher temperatures, exceeding 10 K, a developing homogeneous exchange narrowed line does not provide sufficient absorption lengths $\alpha_e$ to reveal the opposite type of frequency-pulling effects.[9] Reduction of Boltzmann population factor, in spite of a narrower line, accounts for the reduction in $\alpha_e$.

Individual pulse spectrum shapes in Fig. 18 indicate changing average frequency shifts $\omega + \langle\dot{\varphi}(z)\rangle$ as the spin-resonance frequency $\omega_0$ is varied from $\omega_0 < \omega$ through exact resonance $\omega_0 = \omega$ to $\omega_0 > \omega$. The signal obtains from a Teflon tube configuration where $\alpha_e L = 6.5$. When the condition $\omega_0 - \omega \approx 1/\tau$ applies, the hump of the pulse spectrum leans farthest to the right for $\omega_0 < \omega$, and farthest to the left for $\omega_0 > \omega$. A plot of measured values of $\langle\dot{\varphi}(L)\rangle$ vs $\Delta\omega_0$ in Fig. 19 indicates the expected change in sign of $\langle\dot{\varphi}(L)\rangle$. In the limit $L \ll \alpha_e^{-1}$ the maximum value $\langle\dot{\varphi}\rangle_m$ at $(\Delta\omega_0)_m$ from Eq. (31) would be given by

$$(\Delta\omega_0)_m = 1/S\tau\sqrt{2},$$

but the experiment yields $d\langle\dot{\varphi}\rangle/dz$ at $z = L = 6\alpha_e^{-1}$. A numerical integration of Eq. (30) was carried out to account for changes in the pulse spectral shape (fixed as Gaussian only at $z = 0$) at the condition $\alpha_e L = 6$. The data of Fig. 19 was then closely confirmed yielding

$$(\Delta\omega_0)_m\big|_{z=L=6\alpha_e^{-1}} \simeq 3.1 \pm 0.3 \text{ MHz}.$$

Experimental parameters $\tau^{-1} = 4$ MHz (using a filtered pulse) and $T_2^{*-1} = 10$ MHz yield $(\Delta\omega_0)_m|_{z=0} = 3.5 \pm 0.3$ MHz for the analytical case from Eq. (31). These same parameters in the numerical case from Eq. (30) gave an even better fit to the data.

In accord with Eq. (33), bell-shaped pulses (although not hyperbolic-secant shaped) that have input areas near $2\pi$ yielded greatly diminished measured derivatives $d\langle\dot{\varphi}(L)\rangle/dz$ compared to derivatives resulting from input areas near $\pi$, as shown in Fig. 19. Computer simulation and pulse breakup effects in previous investigations[16] reveal a

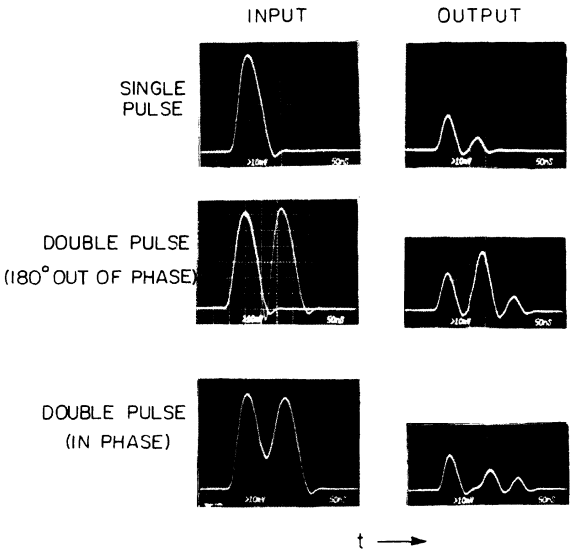


FIG. 17. Small zero-area constructed input pulses compared to the output (0.05 μsec/div). A single input pulse shows the usual spontaneous zero-area output, with $\tau/T_2^* \approx 1.5$. Two such pulses in succession (bottom) with no 180° phase shift at center ($\tau/T_2^* \approx 3$ roughly) exhibit more absorption than the center output signal that results from the constructed 180° phase shift between two successive pulses at the input.

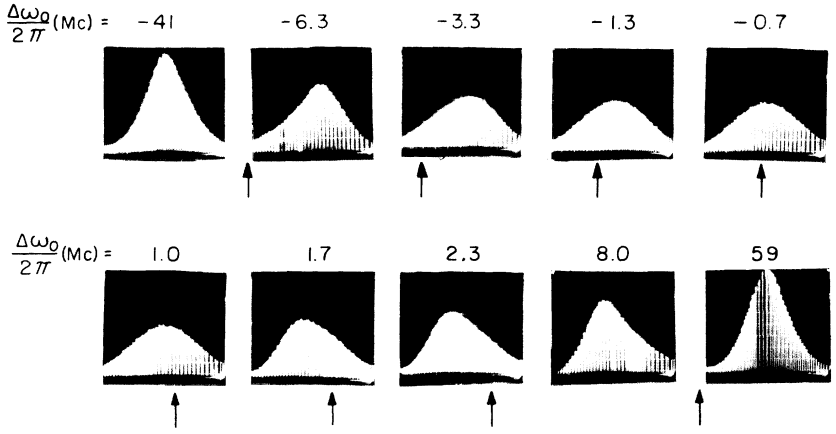


FIG. 18. Output pulse spectral shapes from input pulses applied off-resonance ($\Delta\omega_0 \neq 0$). Spectral sweep: 11 MHz full scale, with $\theta_0 = 1.3$ for all input pulses, and $\alpha_e L = 6.5$ (on-resonance). Arrows indicate spin-resonance line center at $\omega_0$, not assigned to plots for $\Delta\omega_0/2 = -41$ MHz and +59 MHz far off-resonance.

related behavior in which off-resonance input pulses with areas not close to $2\pi$, become reshaped into final stable $2\pi$ hyperbolic-secant pulses in the plane-wave limit while revealing a considerable amount of frequency shift during propagation.

## IX. CONCLUSIONS

Waveguide microwave propagation of submicrosecond pulses in a two-level electron EPR system reveals novel as well as generally known properties of SIT. New observations of spectral and off-resonance characteristics of SIT are made possible by the accuracy of microwave techniques. The magnetic-moment–microwave-field interaction is directly involved where the Bloch-Maxwell equations literally apply. The form of these equations was originally applicable to optical electric dipole SIT experiments. Waveguide microwave mode is of primary importance in determining modified forms of the area theorem and may be controlled over the sample by choice of sample geometry in the waveguide. Experiment confirms that a given mode remains essentially invariant during pulse propagation, and that a dynamic feedback between two-level dipole oscillators and the waveguide structure is represented in terms of a chosen mode function. Only the previous case[7] of neon-helium ring mode-locked laser-pulse characteristics has been confirmed by the SIT mode profile formalism.

The flexibility of microwave-pulse measurements in the time and frequency domain has permitted studies of anomalous pulse propagation as a smooth function of input pulse power, area, and carrier frequency relative to the spin-resonance frequency. Computer-predicted pulse delays of a few input pulse widths and predicted output pulse areas exceeding input areas are inhibited in the experiment by pulse source frequency modulation, spin-relaxation damping, and spatial variations of the polarizing field over the helical sample. Changes in effective sample absorption lengths were imposed by variation of sample temperature, and therefore of the Boltzmann spin population difference. Spontaneous zero-area pulse propagation has been obtained in which input pulses, of spectral width comparable to spin resonance widths, develop a reduced Fourier amplitude at the center of the line with increase of propagation distance. Anomalous propagation therefore takes place over distances exceeding classical absorption lengths. While a spontaneous zero-area pulse develops during propagation, a spectral hole filling process takes place before the onset of SIT. This effect provides a unique signature for the SIT effect when the input pulse spectral width is

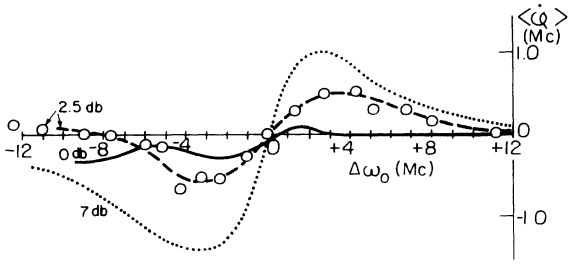


FIG. 19. Average frequency shift ($\dot{\phi}$) of the pulse spectrum as a function of off-resonance parameter $\Delta\omega_0$ for several input areas $\theta_0$. The input $\theta_0 = 1.3\pi$ of Fig. 18 corresponds to data of the 7-db curve. The other curves pertain to $\theta_0 = 2.2\pi$ (2.5 db) and $\theta_0 = 2.9\pi$ (0 db), which are relatively close to $\theta_0 = 2\pi$, and show less frequency pushing according to Eq. (33).

comparable to or greater than the resonance linewidth. Anomalous changes of pulse carrier frequency toward the resonance line center in the nonlinear regime during propagation are confirmed for pulses applied off-resonance, as predicted for inhomogeneously broadened two-level absorbers.

Our investigation suggests that similar waveguide modified SIT effects would occur in fiber optical waveguides. Even if such guides contain optical absorbers characterized by a band of degenerate levels distributed over a band of frequencies, instead of by a well defined two-level system, anomalous propagation will occur for pulse durations less than the induced dipole damping times. Anomalous propagation, although complicated by spin-wave modes, would also occur for traveling-wave ferromagnetic resonance in a waveguide.

## APPENDIX A

The slowly-varying-envelope approximation for the traveling-microwave magnetic-dipole-field interaction is obtained from the wave equation

$$\left(\nabla_t^2+\frac{\partial^2}{\partial z^2}+\frac{\eta^2}{c^2}\frac{\partial^2}{\partial t^2}\right)\vec{H}_t = 4\pi[\nabla^2\vec{M}-\nabla(\nabla\cdot\vec{M})], \quad \text{(A1)}$$

where $\nabla_t^2=\partial^2/\partial x^2+\partial^2/\partial y^2$. With $\vec{H}_t$ defined by (1), the constraint of a single mode function $\hat{\xi}(x,y)$ is obtained by taking the dot product of complex conjugate $\xi^*(x,y)$ with (A1), integrating over the mode cross section ($dA=dx\,dy$), and applying mode normalization [Eq. (7)]. Equation (A1) reduces to the first-order forward-traveling wave equation

$$-2ik_g e^{i(\omega t-k_g z)}\left(\frac{\partial h_t}{\partial z}+\frac{\eta\omega^2}{k_g c^2}\frac{\partial h_t}{\partial t}\right) = 4\pi\int\int dA\,\hat{\xi}^*\cdot[\nabla^2\vec{M}-\nabla(\nabla\cdot\vec{M})]. \quad \text{(A2)}$$

The basic $TE_{10}$ mode for an empty guide is not seriously distorted in the presence of a sample. We may therefore apply it in order to illustrate the field components peculiar to a waveguide in the rotating frame. At a point $x,y$, the mode vector function $\hat{\xi}$ must also express the microwave-field dependence upon the elliptical polarization determined by components $h_y$ and $h_z$ in the $yz$ plane. Therefore,

$$\hat{\xi}(x,y)=\hat{x}\xi_x+\hat{y}\xi_y+\hat{z}\xi_z,$$
$$h_x=\xi_x=0,$$
$$h_y=h\xi_y=-(hk_g dC/\pi)\sin(\pi y/d),$$
$$h_z=h\xi_z=-iC\cos(\pi y/d),$$
$$C=\left(\frac{2}{sd(1+d^2k_g^2/\pi^2)}\right)^{1/2}.$$

The imaginary axis is defined along $z$; $d$ and $s$ are the waveguide internal dimensional width and height, respectively.

The transverse induced magnetization is defined as

$$\vec{M}=\hat{y}M_y+\hat{z}M_z=(M_y+iM_z)\hat{q}_-+(M_y-iM_z)\hat{q}_+,$$

where $\hat{q}_\pm=\hat{y}\pm i\hat{z}$.

Electron-spin precession for $\gamma_e=-\gamma$ corresponds to the choice of

$$\vec{M}=\vec{M}_+=(M_y+iM_z)\hat{q}_-=\hat{q}_-(u+iv)e^{i(\omega t-kz+\varphi)}=\hat{q}_-Qe^{i(\omega t-kz)}$$

as the rotating magnetization applicable to (A2), where $Q$ is defined in Eq. (4). In (A2) therefore the first term on the right-hand side reduces to

$$\nabla^2\vec{M}_+=(\partial^2/\partial y^2-k_g^2)\vec{M}_+=-(\gamma_m^2+k_g^2)\vec{M}_+. \quad \text{(A3)}$$

Since $\vec{M}_+$ has the spatial dependence $e^{-ik_g z}$. The result (A3) follows from the mode condition (Sec. II)

$$(V_t^2+\gamma_m^2)\vec{M}_+=(\partial^2/\partial y^2+\gamma_m^2)\vec{M}_+=0,$$

where

$$\gamma_m^2+k_g^2=\eta^2\omega^2/c^2.$$

The second term on the right-hand side is an integral over

$$\xi^*\cdot\nabla(\nabla\cdot\vec{M})=\xi_z^*\frac{\partial\nabla\cdot\vec{M}}{\partial z}+\xi_y^*\frac{\partial\nabla\cdot\vec{M}}{\partial y}.$$

This can be reduced by assuming a $z$ dependence of $\vec{M}$ of $e^{-ik_g z}$ and using the relationship between the components of the mode[10]

$$\hat{\xi}_y^*=\frac{ik_g}{\gamma_m^2}\frac{\partial\xi_z^*}{\partial y}.$$

Integration by parts using the mode relation for $\partial^2 M/\partial y^2$, and reversing the order of the derivatives results in a cancellation of all but the surface term

$$-4\pi b\,\frac{ik_g}{\gamma_m^2}\frac{\partial\xi_z^*}{\partial y}\nabla\cdot\vec{M}\Big|_0^d.$$

This term is identically zero by the boundary condition defining a TE mode[17]

$$\left.\frac{\partial B_z}{\partial n}\right|_S=0.$$

Thus, the second term on the right-hand side of (A2) reduces identically to zero. Equation (A2) becomes

$$\frac{\partial h_t}{\partial z}+\frac{\eta^2\omega}{k_g c^2}\frac{\partial h_t}{\partial t}=-\left(\frac{2\pi i\eta^2\omega^2}{k_g c^2}\right)\int_S dA\,\hat{\xi}^*\cdot\hat{q}_-\times\int_{-\infty}^{\infty}Q(\delta)g(\delta)\,d\delta. \quad \text{(A4)}$$

The rotating microwave-field modulus is

$$h(y) = h(\hat{\xi} \cdot \hat{q}_+)$$
$$= hC\left[\cos\left(\frac{\pi y}{d}\right) - \frac{k_g d}{\pi}\sin\left(\frac{\pi y}{d}\right)\right]$$

at regions $y$ of the rectangular sample between $y_1$ and $y_2$. Empirical expressions for $h(y)$ as given by Eqs. (20) or (22) take into account distortion of the ideal $TE_{10}$ mode. Where the guide is not occupied by the sample, the form of the mode is of no importance in computer evaluations of areas $\theta_m(z)$ or of field amplitudes $h(z,t)$ at the output ($z = L$) of the guide. All areas contain the common normalization factor $C$ or $CC'$; and the empirically measured absorption coefficient $\alpha_e$ allows a measurement of this factor.

In the absence of a sample ($\vec{M} = 0$) the pulse velocity in the waveguide is

$$V = \frac{c^2 k_g}{\omega\eta^2} = \frac{k_g}{(k^2+\gamma_m^2)^{1/2}}\frac{c}{\eta} .$$

At sample EPR resonance the effect of the mode upon SIT is to cause a spread of component-like pulse delay times from different regions of the sample.

## APPENDIX B

By considering an input pulse shape of the form

$$h_n(0,t) = h_0(t/\tau)^n e^{-t/\tau} ,$$

where $n = 0, 1, 2, \ldots$, the pulse energy is obtained[8] from a linear analysis in terms of the pulse Fourier transform $\tilde{h}_n(z,\nu)$ as

$$\mathcal{T}_n(z) = \int_{-\infty}^{\infty} \tilde{h}_n(z,\nu)\tilde{h}_n^*(z,\nu)\,d\nu$$
$$= \frac{h_0^2(n!)^2}{\tau^{2n}} \frac{\int_{-\infty}^{\infty} d\nu \exp[-\alpha_e z/(1+\nu^2 T_2^{*2})]}{(\nu^2+\tau^{-2})^{n+1}} . \tag{B1}$$

The effective absorption coefficient $\alpha_e$ is applied here which includes the effect of the waveguide mode. For the case $T_2^* \simeq \tau$, substitution of $\tan\xi = \nu T_2^*$ into Eq. (B1) gives

$$\mathcal{T}_n(z) = h_0^2(n!)^2 T_2^* \int_{-\pi/2}^{+\pi/2} d\xi(\cos^{2k}\xi)\exp(-\alpha_e z\cos^2\xi) . \tag{B2}$$

From Eq. (B2) the analytic expression for $n = 0$ has been obtained[8]:

$$\mathcal{T}_0(z) = h_0^2 T_2^* \pi e^{-\alpha_e z/2} I_0\left(\frac{\alpha_e z}{2}\right) , \tag{B3}$$

where $I_0(\frac{1}{2}\alpha_e z)$ is the zero-order Bessel function with an imaginary argument. In addition, we obtain the analytic pulse energy expression for $n = 1$ by noting first that Eq. (B2) can be written as

$$\mathcal{T}_n(z) = (n!)^2\left(-\frac{1}{\alpha_e}\right)^n \frac{d^n}{dz^n}\{\mathcal{T}_0(z)\} . \tag{B4}$$

Combining (B1) and (B3) with (B4) gives

$$\mathcal{T}_n(z) = \frac{\mathcal{T}_n(0)(n!)^2 2^{2n}}{(2n)!}\left(-\frac{1}{\alpha_e}\right)^n \frac{dn}{dz^n}[e^{-\alpha_e z/2} I_{0\frac{1}{2}}\alpha_e z] , \tag{B5}$$

where $\mathcal{T}_n(0)$ is given by Eq. (B1) defined at $z = 0$. For $n = 1$, Eq. (B5) becomes

$$\mathcal{T}_1(z) = \mathcal{T}_1(0)e^{-\alpha_e z/2}[I_0(\tfrac{1}{2}\alpha_e z) - I_1(\tfrac{1}{2}\alpha_e z)] ,$$

which now involves $I_1(\frac{1}{2}\alpha_e z)$ as the first-order Bessel function of imaginary argument. For large $z$ the asymptotic behavior of $I_0(\frac{1}{2}\alpha_e z)$ given by

$$I_0(\tfrac{1}{2}\alpha_e z) \to e^{-\alpha_e z/2}/(2\pi\alpha_e z)^{1/2} .$$

leading to the asymptotic pulses energy behavior of Eq. (B5) as

$$\mathcal{T}_n(z) \to \mathcal{T}_n(0) n!\sqrt{\pi}\,(1/\alpha_e z)^{n+1/2} .$$

---

*Supported by the National Science Foundation.

†Submitted in partial fulfillment of the requirements for the degree of Ph.D.

[1]S. L. McCall and E. L. Hahn, Phys. Rev. 183, 457 (1969).

[2]F. Bloch, Phys. Rev. 70, 460 (1946).

[3]R. P. Feynman, F. L. Vernon, Jr., and R. W. Hellwarth, J. Appl. Phys. 28, 48 (1957).

[4]S. B. Grossman and E. L. Hahn, Bull. Am. Phys. Soc. 18, 1572; *Proceedings of the Colloque Ampere Conference, Krakow, Poland,* edited by J. Hennel (Institute of Nuclear Physics, Krakow, 1973), p. 63.

[5]J. C. Diels and E. L. Hahn, *Third Rochester Conference on Coherence and Quantum Optics, 1972,* edited by L. Mandel and E. Wolf (Plenum, New York, 1973), p. 1; J. P. Grieneisen, J. Goldhar, and N. A. Kurnit, *ibid.*, p. 5; A. Szoke, J. Goldhar, H. P. Grieneisen, and N. A. Kurnit, Opt. Commun. 6, 131 (1972); J. C. Diels and E. L. Hahn, Phys. Rev. A 10, 2501 (1974).

[6]N. S. Shiren, Phys. Rev. B 2, 2471 (1970).

[7]S. L. McCall and E. L. Hahn, Phys. Rev. A 2, 861 (1970).

[8]M. D. Crisp, Phys. Rev. A 1, 1604 (1970).

[9]J. C. Diels and E. L. Hahn, Phys. Rev. A 8, 1084 (1973).

[10]J. D. Jackson, *Classical Electrodynamics* (Wiley, New York, 1962), Chap. 8, pp. 235–267.

[11]T. M. Pierce and E. L. Hahn, Bull. Am. Phys. Soc. 17, 47 (1972).

[12]E. L. Hahn, N. S. Shiren, and S. L. McCall, Phys. Lett. 37A, 265 (1971).

[13]J. P. Goldborough, M. Mandel, and G. E. Pake, Phys. Rev. Lett. 4, 13 (1960).

[14]W. O. Hamilton and G. E. Pake, J. Chem. Phys. 39, 2694 (1963).

[15]B. Lax and K. J. Button, *Microwave Ferrites and Ferromagnetics* (McGraw-Hill, New York, 1962).
[16]J. C. Diels and E. L. Hahn, Phys. Rev. A 10, 2501 (1974).
[17]Reference 10, p. 243. Even for a partially filled waveguide, the same result can be rederived by employing a theta function.

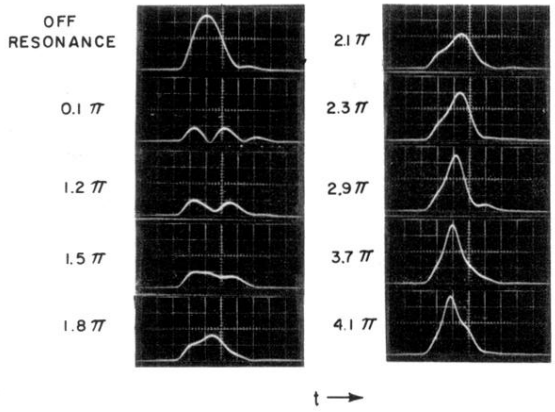


FIG. 10. Nonlinear output pulse shapes in the time domain, identical to conditions of Fig. 4, except that $\tau \approx T_2^*$ here. Spontaneous zero-area pulse oscillations are evident for $\theta_0 = 0.1\pi$ and $1.2\pi$.

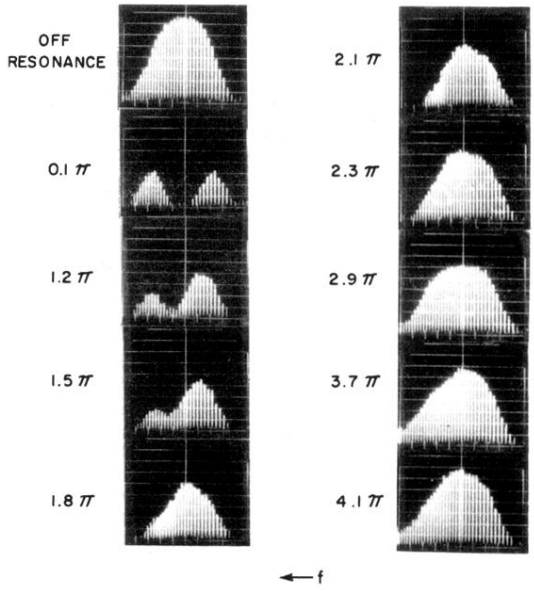


FIG. 11. Corresponding pulse Fourier spectra of Fig. 10 pulse time domain pulse shapes (20 MHz full scale). For small $\theta_0$, the hole filling of the spectrum at $\Delta\omega_0 \sim 0$ indicates spontaneous zero-area pulse disappearance as SIT develops for increasing $\theta_0$. Frequency shift in the dip of the spectrum is caused by effects of magnetron frequency modulation and slight asymmetry in BDPA spin-resonance line shape.

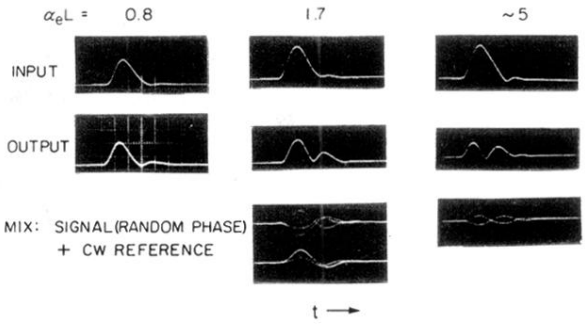


FIG. 14. Approach of propagating pulse toward a spontaneous zero-area pulse in the time domain (0.05 $\mu$sec/div) for $\tau/T_2^* \approx \frac{1}{3}$. For larger absorption lengths $\alpha_e L$, the buildup of zero-area oscillations occurs. Input and output pulse shapes are compared. For $\alpha_e L = 1.7$ and 5, a constant reference signal mixed with the output pulse shows interference at random phase with respect to the output pulse indicating 180° phase shifts between absorption and emission portions of the pulse.

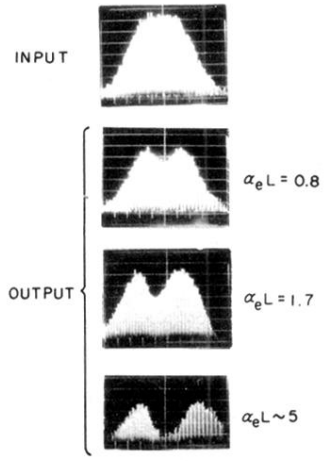


FIG. 15. Spectral behavior of spontaneous zero-area pulse propagation (20 MHz full scale). Corresponding to Fig. 14, the output pulse spectra develop a deeper cusp at $\Delta\omega_0 \approx 0$ for increasing $\alpha_e L$.

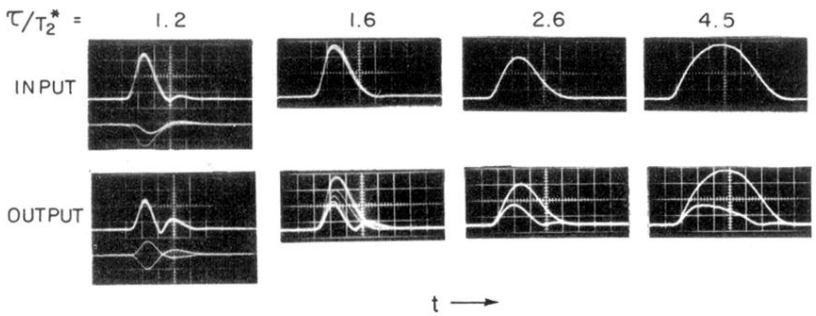


FIG. 16. Change of output pulse in time domain (0.05 $\mu$sec/div) from spontaneous zero area to classical absorption, as $\tau/T_2^*$ is increased. These spectral outputs correspond to the time-domain outputs of Fig. 9.

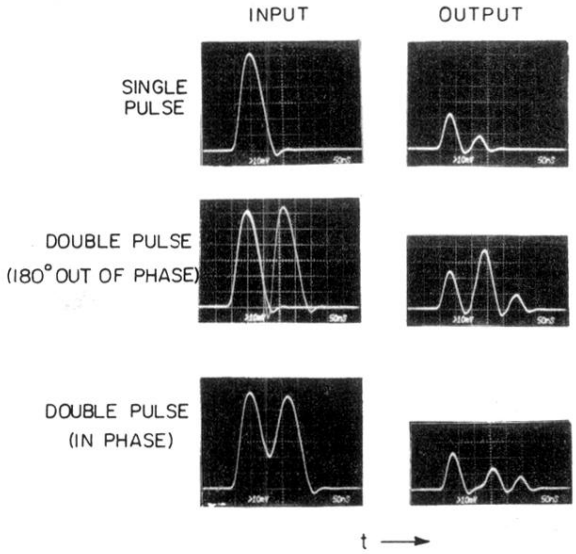


FIG. 17. Small zero-area constructed input pulses compared to the output (0.05 $\mu$sec/div). A single input pulse shows the usual spontaneous zero-area output, with $\tau/T_2^* \approx 1.5$. Two such pulses in succession (bottom) with no 180° phase shift at center ($\tau/T_2^* \approx 3$ roughly) exhibit more absorption than the center output signal that results from the constructed 180° phase shift between two successive pulses at the input.

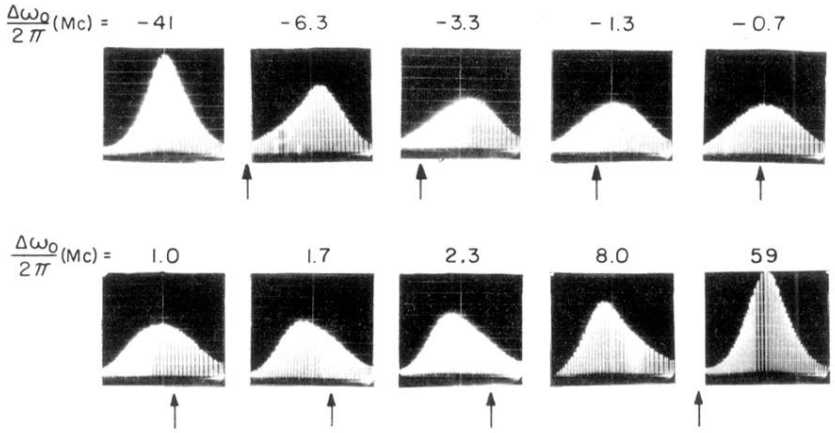


FIG. 18. Output pulse spectral shapes from input pulses applied off-resonance ($\Delta\omega_0 \neq 0$). Spectral sweep: 11 MHz full scale, with $\theta_0 = 1.3$ for all input pulses, and $\alpha_e L = 6.5$ (on-resonance). Arrows indicate spin-resonance line center at $\omega_0$, not assigned to plots for $\Delta\omega_0/2 = -41$ MHz and +59 MHz far off-resonance.

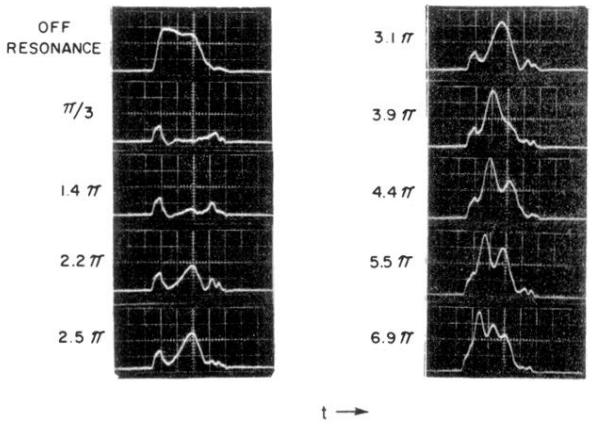


FIG. 3. Nonlinear output pulses at exact resonance ($\Delta\omega_0 = 0$) in the time domain (0.05 $\mu$sec/div) for the tube waveguide geometry with $\alpha_e L \approx 5.5$. Vertical output signals from the diode (Fig. 2) are proportional to $h(L, t)$, which determine $\theta$, and are labeled by input areas $\theta_0$, from which $\theta$ evolves. All $\theta_0$ obtain from the input pulse shape $h(0, t)$ shown at the top left. All output signals $h(L, t)$ obtain from input signals $h(0, t)$ adjusted to the same amplitude on the oscilloscope. Multiple-pulse break-up characteristic of SIT appears for the highest input areas. With no NBPF (Fig. 2), ragged pulse edges in the output are caused mostly by nonresonant spectral wings, frequency modulation in the magnetron pulse input, and deviation from exact sample resonance because of $H_0$ spatial variations over the helix geometry.

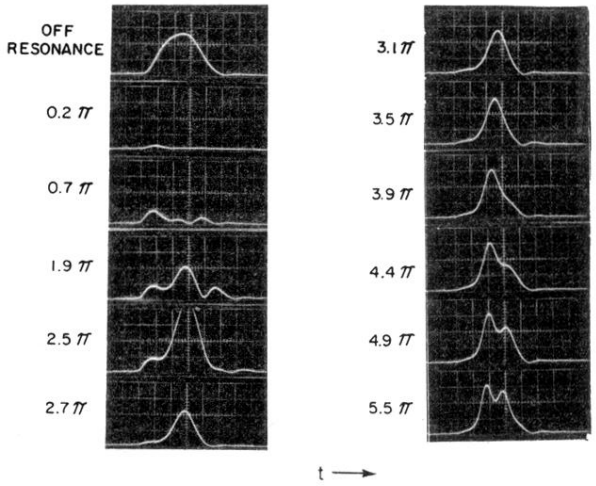


FIG. 4. Nonlinear output pulses with narrow-band pass filter (NBPF, Fig. 2) switched in. The conditions otherwise are the same as in Fig. 3 except for a different sequence of input areas $\theta_0$. SIT characteristics are seen as in Fig. 3 with pulse symmetrization more evident. Signals corresponding to $\theta_0 = 0.7\pi$, $1.9\pi$, and $2.5\pi$ are multiplied by a gain factor 2.8 relative to the remaining normalized signals.

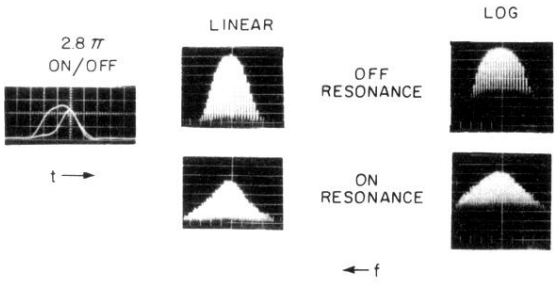


FIG. 7. Spectral pulse shape of output vs input pulse. At left the pulse shape on- and off-resonance (0.05 μsec/div) shows the on-resonance pulse symmetrized and shorter than the superimposed off-resonance pulse. The Gaussian character of the input (off-resonance) pulse is altered toward the Lorentzian character of the on-resonance pulse. These pulses show spectral amplitudes in the wings proportional to $e^{-t}$ (linear) and $t$ (log), respectively.

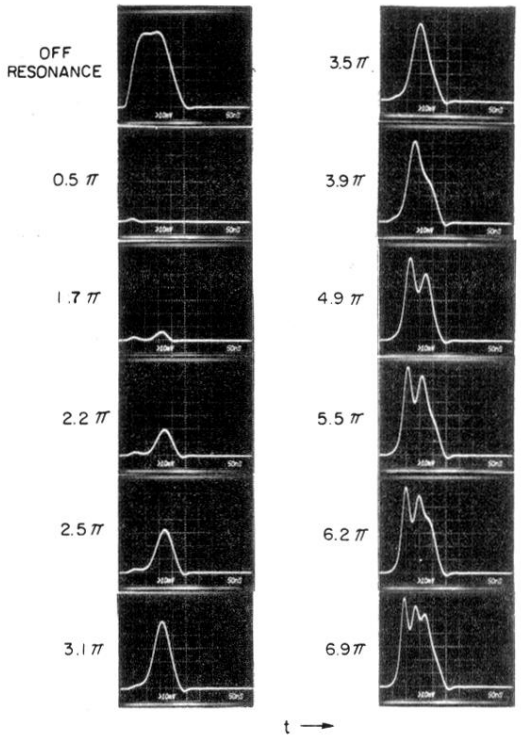


FIG. 8. Nonlinear output pulses in the time domain for the half-filled waveguide geometry with $\alpha_e L = 4.5$. Conditions otherwise are similar to those of Fig. 4, with pulse break-up evident.

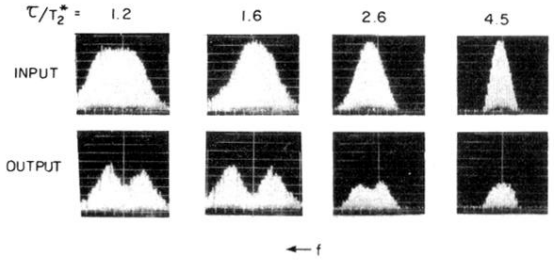


FIG. 9. Input and output weak-pulse spectra compared for various ratios of pulse width to inverse spin spectrum width ($\tau/T_2^*$). For increasing $\tau/T_2^*$ the change from spontaneous zero-area regime to the Beer's-law regime occurs. (Corresponding time-domain plots are shown later in Fig. 16.) $\alpha_e L = 2.2$ for all signals.